nature communications

Article

https://doi.org/10.1038/s41467-025-65604-3

Low resistance *p*-type contacts to monolayer WSe_2 through chlorinated solvent doping

Received: 24 March 2025

Accepted: 20 October 2025

Published online: 20 January 2026

Check for updates

Lauren Hoang[1], Robert K. A. Bennett[1], Anh Tuan Hoang[2], Tara Peña[1], Zhepeng Zhang[2], Marisa Hocking[2], Ashley P. Saunders[3], Marc Jaikissoon[1], Fang Liu[3], Eric Pop[1,2,4] & Andrew J. Mannix[2]

Tungsten diselenide (WSe_2) is a promising *p*-type semiconductor limited by high contact resistance (R_C) and the lack of a reliable doping strategy. Here, we demonstrate that exposing WSe_2 to chloroform provides simple and stable *p*-type doping. In monolayer WSe_2 transistors with Pd contacts, chloroform increases the maximum hole current by over 100× (>200 μA/μm), reduces R_C to ~ 2.5 kΩ·μm, and retains an on/off ratio of 10^{10} at room temperature. These improvements persist for over 8 months, survive a 150 °C thermal anneal, and remain effective down to 10 K, enabling a cryogenic R_C of ~ 1 kΩ·μm. Density functional theory indicates that chloroform strongly physisorbs to WSe_2, inducing hole doping with minimal impact on the electronic states between the valence band and conduction band edges. Auger electron spectroscopy and atomic force microscopy suggest that chloroform intercalates at the WSe_2 interface with the gate oxide, contributing to doping stability and mitigating interfacial dielectric disorder, though further studies are needed to conclusively confirm this mechanism. This robust, scalable approach enables high-yield WSe_2 transistors with good *p*-type performance.

Two-dimensional (2D) semiconductors, particularly transition metal dichalcogenides (TMDs), are promising candidates for next-generation, high-density, complementary-metal-oxide-semiconductor (CMOS)[1,2] and low-temperature electronics. However, the large contact resistance (R_C) often observed in nanoscale TMD devices poses a significant obstacle to device performance, limiting the on-state drain current, I_D, needed for practical circuit applications. Both *n*-type and *p*-type transistors are critical for low-power CMOS[3], but progress on minimizing R_C has largely been limited to *n*-type devices[4,5]. Developing scalable, low-R_C *p*-type contacts for 2D transistors remains a critical challenge. Additionally, R_C typically increases further at low temperatures, impeding other fundamental charge transport studies[6].

Various strategies have been explored to reduce R_C to *p*-type WSe_2 transistors, including transferred metal[7] or semimetal[8,9] contacts. However, metal contacts typically form large Schottky barriers at the metal-2D semiconductor interface (preventing low R_C), and semimetal contacts have yet to experimentally demonstrate superior performance for *p*-type devices. An alternative is to lower R_C by implementing stable *p*-type doping near the contacts. Substitutional doping with electron acceptors (e.g., V[10], Nb[11,12]) is stable due to covalent chemical bonding but is likely to require complex fabrication with multiple material growth steps. In comparison, *p*-type surface charge transfer doping (SCTD)[13–24] withdraws electrons from the 2D channel using higher electronegativity capping or adsorbate layers with work function values below the Fermi-level of the WSe_2, such as transition metal oxides (MoO_x[13] and WO_x[14,17,18]), NO_x[19,20,25,26], and halide compounds ($HAuCl_4$[21], $AuCl_3$[22], $RuCl_3$[23,24], $PtCl_4$[16]). SCTD typically preserves the host lattice and has the potential to introduce fewer scattering centers[27]. However, the temporal and thermal stability of these methods remains unclear due to the high chemical reactivity or low thermal stability of the reagents involved[28]. Furthermore, there is little consensus on the mechanism of halide-based doping, with some studies

[1]Department of Electrical Engineering, Stanford University, Stanford, CA, USA. [2]Department of Materials Science and Engineering, Stanford University, Stanford, CA, USA. [3]Department of Chemistry, Stanford University, Stanford, CA, USA. [4]Department of Applied Physics, Stanford University, Stanford, CA, USA. e-mail: ajmannix@stanford.edu

suggesting reactions in which Cl atoms substitute and passivate chalcogen vacancies[29–31], while others propose molecular physisorption[22,32] or intercalation[33].

Solvent exposure can also unintentionally dope TMDs. For example, MoS_2 and WSe_2 are *n*-doped by exposure to the low-electronegativity solvent acetone during removal of electron-beam (e-beam) lithography resists like poly(methyl methacrylate) (PMMA)[34,35]. Conversely, the high-electronegativity solvent chloroform ($CHCl_3$) was shown to *p*-dope semimetallic graphene[33]. This suggests that chloroform could serve as an effective *p*-type dopant for 2D semiconductors such as WSe_2, offering a simple and scalable approach compared to existing doping techniques. However, solvent-based doping is often regarded as transient, and the impact of chloroform doping on the electrical performance of *p*-channel WSe_2 transistors has not yet been studied.

In this work, we demonstrate that chloroform can induce high-performance, stable, and high-yield *p*-doping in monolayer WSe_2 transistors (Fig. 1a, b). Exposing monolayer WSe_2 transistors to chloroform increases I_D by two orders of magnitude, with hole currents reaching up to 203 µA/µm at $V_{DS} = -1$ V (Fig. 1c). These devices also maintain large I_{on}/I_{off} ratios (~10^{10}) and a low R_C of 2.5 kΩ·µm (at room temperature) and 1.0 kΩ·µm (at 10 K). Compared to recent approaches such as contact engineering (e.g., Sb/Pt[8,36], Ru[37,38]), oxide-based doping (WO_x[17,39], MoO_x[8,40], NO_x[19,39]), and other halide-based dopants ($HAuCl_4$[21], $RuCl_3$[23]), chloroform doping achieves one of the highest reported values for *p*-type transistor current (Fig. 1b). Additionally, we observe that chloroform-doped transistors remain stable over 8 months (retaining 81% of initial doped $I_{D,max}$) and survive annealing at 150 °C. Density functional theory (DFT) reveals that chloroform binds strongly (> 260 meV, i.e., >10k_BT at 296 K) to WSe_2 without introducing mid-gap states. Atomic-force microscopy (AFM), Auger electron spectroscopy (AES), and X-ray photoelectron spectroscopy (XPS) suggest that chloroform intercalates at the WSe_2 interface with the gate oxide, further stabilizing its doping. This straightforward approach enhances *p*-type performance in WSe_2 transistors and complements other contact and interface engineering techniques for advancing 2D semiconductor technologies.

Results and discussion

Characterization of chloroform-doped WSe_2

Optical spectroscopy provides insights into the physical and chemical interactions between the WSe_2 and chloroform. Raman spectra of monolayer WSe_2 soaked overnight in chloroform show no significant changes in the E′/A_1′ peak intensity ratio (Fig. 1d), which suggests that long-term chloroform exposure does not significantly increase the WSe_2 defectivity. We also do not observe an increase in LA(M) or

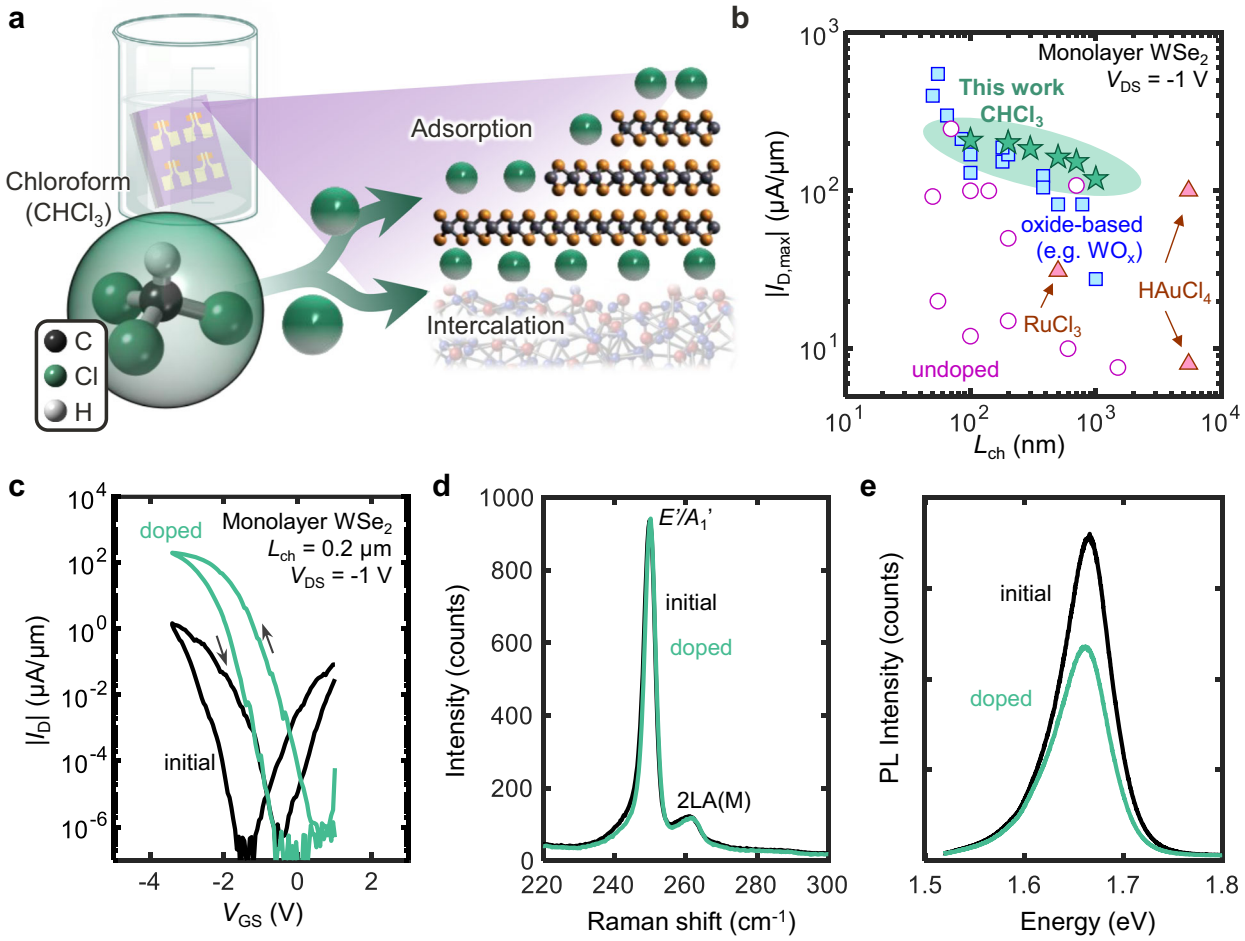

Fig. 1 | *p*-type doping of monolayer WSe_2 using chloroform. a Schematic of chloroform-doped WSe_2, illustrating the doping process and possible adsorption pathways. After fabrication, devices are left in chloroform overnight. **b** Benchmarking maximum *p*-type current ($|I_{D,max}|$) vs. monolayer WSe_2 channel length (L_{ch}) at drain voltage (V_{DS}) = -1 V at room temperature, using various contact metals and doping strategies. Circles[8,37–39,75–81] mark results with no intentional doping, squares[8,17,19,25,36,39,40] denote oxide-based doping (MoO_x, WO_x, NO_x), and triangles[21,23] label halide-based doping. Our results with chloroform doping (stars) achieve among the highest hole currents to date for monolayer WSe_2. **c** Measured drain current (I_D) vs. gate voltage (V_{GS}) for monolayer WSe_2 device before (black line) and after (green line) chloroform doping, reaching hole current of 203 µA/µm. Forward and backward sweeps are shown, revealing some counterclockwise hysteresis. **d** Raman spectra before and after chloroform doping of monolayer WSe_2. **e** Photoluminescence (PL) spectra of monolayer WSe_2 before and after chloroform doping.

2LA(M) peak intensity associated with the disruption of the WSe_2 lattice (Supplementary Fig. 1). The photoluminescence (PL) spectrum after chloroform doping (Fig. 1e) shows lower intensity than for the undoped sample. This PL quenching is consistent with a chloroform-induced increase in the hole concentration, leading to more non-radiative recombination via positive trions[34]. Additionally, the negligible change in surface roughness and morphology after doping indicates that residue adsorption does not play a significant role (Supplementary Fig. 2).

To investigate the electrical performance of chloroform-doped WSe_2, continuous monolayer CVD-grown WSe_2 was transferred onto an array of prefabricated ~5 nm HfO_2 local back gates (Fig. 2a). The local back gates were defined by photolithography and lift-off of 2/8 nm Ti/Pt, followed by thermal atomic-layer deposition of HfO_2 gate dielectric with equivalent oxide thickness of 1.23 nm. The WSe_2 channel was patterned by XeF_2 etching. Fine contact regions were also defined using e-beam lithography with a bilayer PMMA resist stack. Pd/Au (20/20 nm) were deposited by evaporation at ~10^{-7} Torr, followed by lift-off in acetone overnight, then rinsed in isopropanol (IPA). Electrical measurements were conducted in a vacuum at ~10^{-4} Torr. After initial device measurements, the devices were soaked in chloroform for >8 h and re-measured in vacuum (see Methods for more details).

Figure 2b presents the transfer characteristics of 101 transistors before and after *p*-doping at $V_{DS} = -1$ V, with channel lengths (L_{ch}) ranging from 100 nm to 1 µm. Prior to doping, the devices exhibit a highly negative V_T around −2.6 V. After doping, the V_T shifts positively and the maximum I_D uniformly increases by ~100× across all devices, from ~ 1 µA/µm to >100 µA/µm (Fig. 2c). The low device-to-device variation after doping demonstrates the reproducibility of this doping method. Noticeably, the electron branch is strongly suppressed after doping (Fig. 2b). This suppression likely arises from the positive V_T shift from increased hole concentration (thus requiring higher V_{GS} for electron injection) and from the increase in electron Schottky barrier height, which together hinder electron current.

We can further understand the origin of these improvements by examining the effects of chloroform upon the statistical distributions of the maximum hole current $I_{D,max}$ (at $V_{GS} = -3.4$ V) and the on-state hole current I_{on} at a fixed overdrive voltage ($V_{ov} = |V_{GS} - V_T|$), both shown in Fig. 2c. Interestingly, devices of all channel lengths show concurrent increases in max I_D, and in I_{on} at fixed $V_{ov} = 1.3$ V. Evidently, the chloroform doping shifts V_T positively, but the observed increase in I_{on} at fixed V_{ov} in both long- and short-channel devices suggests the improvement is a combined effect of increased mobility and reduced R_C. The maximum transconductance (g_m) of each device shows a 30.5× median increase (from 1.07 to 33 µS/µm) for $L_{ch} = 1$ µm devices (Supplementary Fig. 3a), consistent with this interpretation.

All devices demonstrate a positive V_T shift (V_T extracted at a constant current 10 nA/µm)[41], with a median shift value of 1.0 V (from −2.6 V to −1.6 V), consistent with *p*-doping (Fig. 2d). This V_T shift corresponds to roughly $0.9–1.8 \times 10^{13}/cm^2$ carriers induced from this doping technique (Supplementary Fig. 3b). Precise quantification of the initial doping concentration in the WSe_2 is difficult as fabrication-induced effects (e.g., adsorbates, annealing, processing history, etc.) can alter the concentration. We estimate an initial electron concentration on the order of 10^{12} cm^{-2} prior to doping (see Supplementary Note 1). Thus, upon chloroform doping, the induced hole density of ~10^{13} cm^{-2} can compensate this initial doping and dominate the final carrier concentration, shifting the device to *p*-type operation.

Additionally, unlike other SCTD methods[13,19,21], the chloroform-doped transistors did not exhibit any degradation in off-state current even at the shortest L_{ch} of 100 nm. We extract the R_C of our Pd-contacted doped monolayer WSe_2 devices using the transfer length method (TLM), yielding an R_C of 2.5 (2.8) kΩ·µm for our best (median) pseudo-TLM structure (as described in Methods) (Fig. 2e). In comparison, the initial R_C before chloroform exposure was 168 kΩ·µm (Supplementary Fig. 3c). The improved R_C likely stems from the doping of the WSe_2 region near the contacts, which narrows the metal-semiconductor energy barrier width and enhances the contribution of tunneling[42,43]. We estimate a low Schottky barrier height (SBH) of ~100 meV after doping, consistent with previous theoretical calculations[44]. However, direct extraction of SBH from temperature-dependent data remains challenging due to the small screening length and large contribution of tunneling current across the narrow barrier. Rigorous simulations to extract SBH are an important future topic to understand the R_C improvement in these and other doped WSe_2 devices. Notably, this R_C value represents the best reported for Pd contacts on monolayer WSe_2 and is comparable to the highest-performing contact schemes reported to date (e.g., Sb/Pt with MoO_x doping[36], WO_x and NO doping[39]). Supplementary Table 1 benchmarks the performance of *p*-type monolayer WSe_2, highlighting that our devices achieve state-of-the-art R_C and performance metrics.

Comparison of the subthreshold swing (SS) before and after doping reveals a decrease in SS for the doped devices, down to 81.4 mV/dec from 144 mV/dec at room temperature (Fig. 2f and Supplementary Fig. 3d). This improvement in SS spans the entire subthreshold range of I_D from doping. (Fig. 2f and Supplementary Fig. 3e), which may be due to passivation of interfacial defects and could also explain the increase in mobility[45].

High R_C also limits the operation of WSe_2 transistors at cryogenic temperatures, impeding the study of WSe_2 in quantum transport devices. Chloroform-doped monolayer WSe_2 transistors at 10 K (Fig. 2g) show consistently high hole current across all devices, up to 403 µA/µm at $V_{DS} = -1$ V for $L_{ch} = 0.1$ µm (Supplementary Fig. 4), with relatively linear I_D vs. V_{DS} (Fig. 2h). The cryogenic R_C ~ 1.0 kΩ·µm was extracted from a pseudo-TLM fit to devices ranging from $L_{ch} = 100$ nm to 1 µm (Fig. 2i). To our knowledge, this is the lowest *p*-type R_C reported to date for cryogenic temperatures.

Charge transfer mechanism of chloroform-doped WSe_2

Temperature-dependent PL measurements of WSe_2 before (Fig. 3a) and after (Fig. 3b) chloroform exposure provide additional evidence for charge transfer. In both samples, the peaks at 1.75 eV and 1.71 eV correspond to neutral excitons (X) and trions (T), respectively, with the 40 meV difference matching the reported trion binding energy[46,47]. Additionally, the relative intensity of the trion peak is greater than the exciton peak in the chloroform-exposed WSe_2 (Supplementary Fig. 5), as expected for increased doping[48].

In both doped and undoped WSe_2, the three lower-energy peaks—labeled L1 (~1.67 eV), L2 (~1.64 eV), and L3 (~1.60 eV)—resemble previous reports of excitonic bound states[48] which display sublinear excitation power dependence (Supplementary Fig. 5) and rapidly quench above 100 K[49]. These characteristics are consistent with weakly-bound defect or donor states near the valence band maxima[49,50]. The intensity of the L1, L2, and L3 peaks is significantly higher in the doped sample (Fig. 3a, b), which indicates increased radiative recombination of electrons and holes bound to different sites and could be explained by the Fermi-level moving towards the valence band after chloroform doping[51,52]. The decrease in exciton intensity and emergence of bound states suggest that the passivation of WSe_2 defects is unlikely. Techniques[53–55] that passivate defects commonly exhibit an increase in quantum yield and the suppression of low-energy defect peaks at low temperatures.

To investigate the *p*-doping mechanism, we modeled the interactions between chloroform and WSe_2 using density functional theory (DFT). The chloroform absorption site was determined by relaxation against a rigid 5 × 5 WSe_2 supercell, considering geometries where the hydrogen atom faced towards (H-facing) or away from (Cl-facing) the monolayer WSe_2. Additional computational details are provided in the Methods section.

https://doi.org/10.1038/s41467-025-65604-3

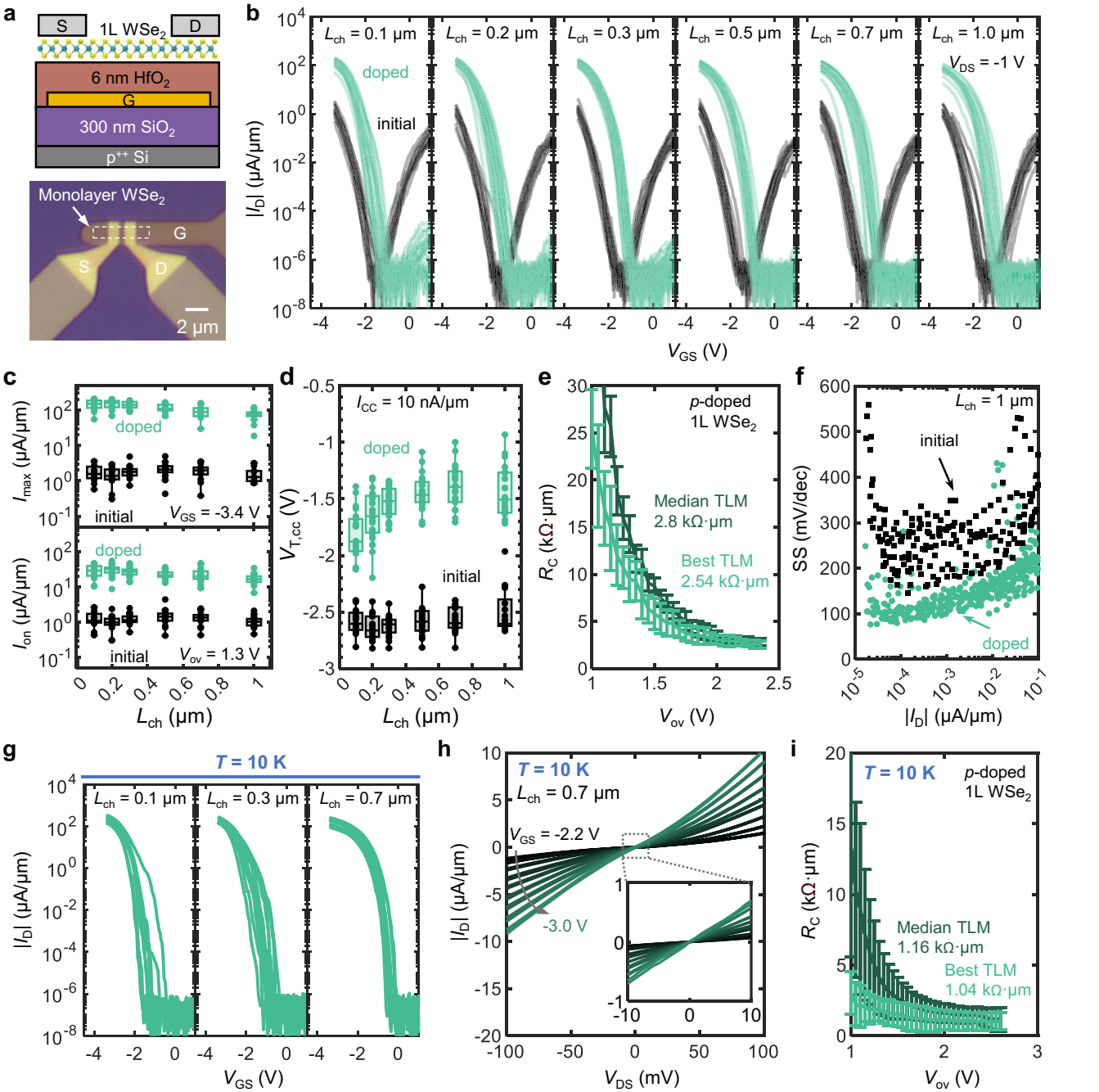

Fig. 2 | Electrical characterization of chloroform-doped monolayer WSe_2 transistors. a Cross-sectional schematic of the WSe_2 transistor (top) and optical microscope image of the fabricated device (bottom). **b** Measured I_D vs. V_{GS} before and after doping at several channel lengths (L_{ch}) from 0.1 to 1 μm. **c** L_{ch}-dependent statistical analysis before and after doping of (top) maximum drain-current $I_{D,max}$ at $V_{GS} = -3.4$ V, and (bottom) on-state current I_{on} at an overdrive voltage $V_{ov} = 1.3$ V. **d** Threshold voltage ($V_{T,cc}$) at a constant current of 10 nA/μm before and after doping. All devices display a positive shift in V_T, indicating *p*-doping. In panels (**c**, **d**), a box plot was created for every group of data. The central mark of the box indicates the median, and the bottom and top edges of the box indicate the 25th and 75th percentiles, respectively. **e** Contact resistance (R_C) of chloroform-doped WSe_2 devices with Pd contacts, extracted using the transfer length method (TLM). **f** Subthreshold swing (SS) vs. I_D in $L_{ch} = 1$ μm devices before and after doping. Doped devices show lower SS across the whole subthreshold I_D range. **g** Measured I_D vs. V_{GS} at 10 K after doping for various channel lengths ($L_{ch} = 0.1$ to 0.7 μm). **h** I_D vs. V_{DS} curve for a representative $L_{ch} = 0.7$ μm device at 10 K from $V_{GS} = -3.0$ V to -2.2 V in steps of 0.1 V increments. The inset shows a magnified view of the low-voltage region. **i** R_C of chloroform-doped WSe_2 devices with Pd contacts at 10 K, extracted using the TLM method. Notably, a low contact resistance and high drain current are still maintained at cryogenic temperatures. In panels (**e**, **i**), error bars indicate the standard error of the linear fit used for TLM extraction (fitting total resistance vs. L_{ch} at fixed V_{ov}), representing the uncertainty in the extracted R_C.

The Cl-facing and H-facing chloroform orientations exhibit favorable adsorption energies (E_{ads}) of −468 and −351 meV, respectively, indicating strong physisorption ($|E_{ads}| \gg k_BT$) to the WSe_2 without inducing covalent chemical modification (Fig. 3c, d). This greatly exceeds adsorption energies between some small molecules and graphene ($|E_{ads}| < 100$ meV)[56] and are on the high end of values calculated for other adsorbates on TMDs (50 to 333 meV)[57,58]. In comparison, chemisorption is characterized by stronger binding energies (≥1 eV) and shorter distances (<2 Å)[59]. Thus, the adsorption energies and equilibrium distance from 2.5–3.2 Å (Fig. 3d) resemble strong physisorption.

https://doi.org/10.1038/s41467-025-65604-3

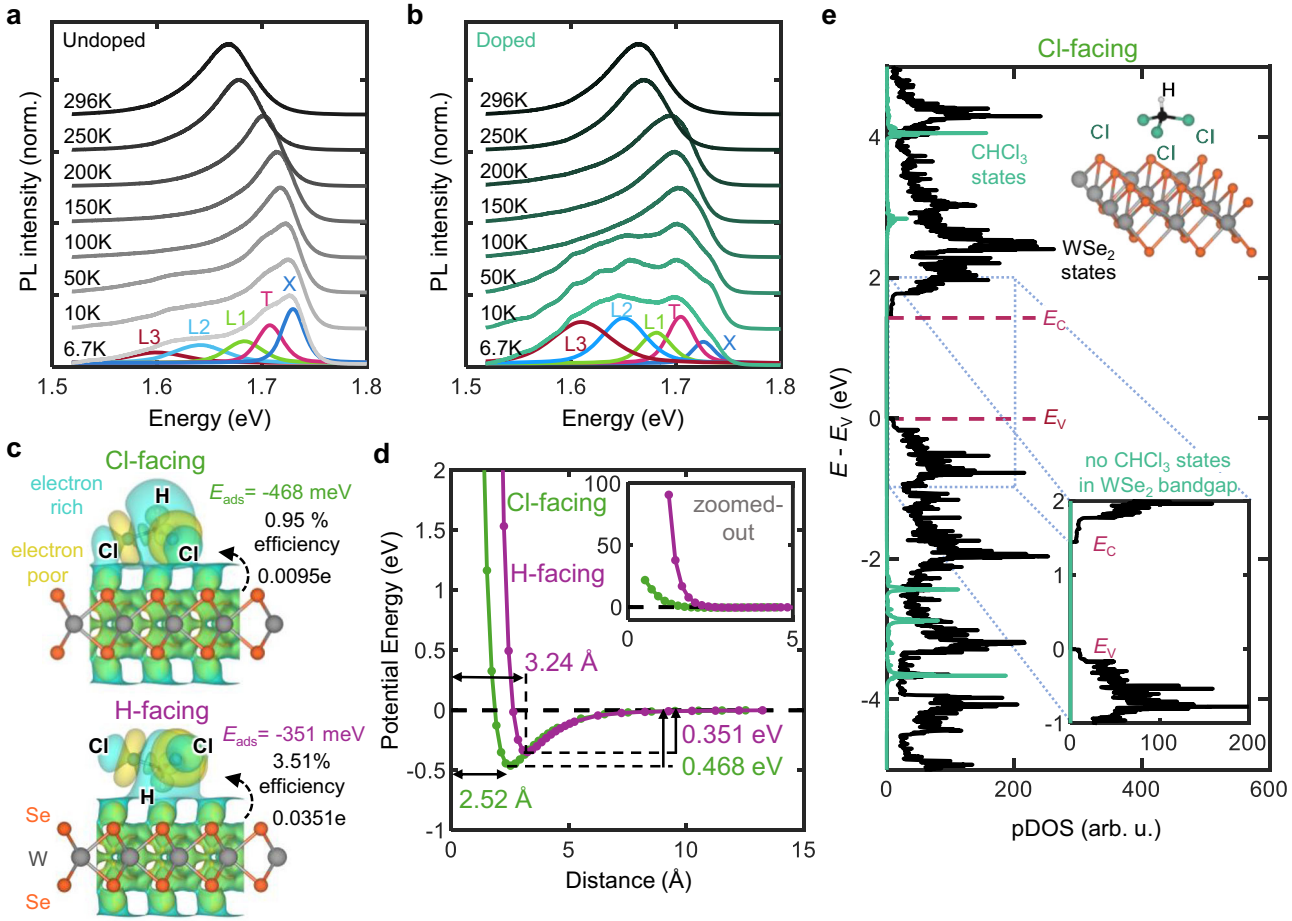

Fig. 3 | Charge transfer mechanism of monolayer WSe_2 doped with chloroform. a Photoluminescence (PL) spectra of an undoped monolayer WSe_2 sample at different temperatures (6.7 to 296 K). **b** PL spectra of chloroform-doped monolayer WSe_2 sample from 6.7 to 296 K. Representative Gaussian-Lorentzian blend curve fits are shown for the 6.7 K spectra in panels (**a**, **b**), corresponding to the neutral exciton (X), trion (T), and L1-L3 peaks (described further in the text). **c** Density functional theory (DFT) simulated isosurfaces of monolayer WSe_2 with adsorbed chloroform in Cl-facing (top) and H-facing (bottom) configurations, as well as the calculated adsorption energies (E_{ads}). The value of the Bader charge transfer efficiency is shown for each chloroform orientation, corresponding to the charge transfer of one chloroform molecule. **d** Potential energy vs. distance for an adsorbed chloroform to monolayer WSe_2 in Cl-facing and H-facing orientations. The adsorption energy ranges from 300–500 meV and the equilibrium distance from 2–4 Å, consistent with strong physisorption. Inset: zoomed-out view of the potential energy vs. distance. **e** Projected density of states (pDOS) contributions from monolayer WSe_2 and chloroform to the overall DOS in the Cl-facing orientation. The valence band maximum E_V and conduction band minimum E_C are marked with dashed pink lines. Noticeably, no chloroform states are formed in the WSe_2 band gap. The inset shows a zoomed-in view of the PDOS contributions around the WSe_2 band gap.

Bader charge analysis reveals that the chloroform withdraws electrons from the WSe_2 in both configurations (Fig. 3c). In both the Cl-facing and H-facing orientations, the adsorbed chloroform molecule gains a net charge of 0.0095 and 0.0351 excess electrons, respectively, confirming *p*-doping. These electron transfers are comparable to that between several well-known TMD SCTD systems, including: (i) MoO_3, a well-established *p*-dopant, and MoS_2 (~0.077 electrons[60] transferred from MoS_2 to MoO_3 per unit cell of MoS_2, assuming full surface coverage), (ii) MoS_2 and acetone (~ 0.039 electrons transferred to MoS_2 per molecule of acetone[61]), which is known to strongly *n*-dope 2D TMDs[34,35], and (iii) nitric oxide (NO) and WS_2 (0.018 electrons per molecule of NO[57]), which is known to be an excellent *p*-dopant for 2D TMDs[19,39]. For a threshold voltage shift of 1 V, the calculated Bader charge transfer of 0.0095 (0.0351) holes per chloroform molecule corresponds to a surface coverage of 1.0 (0.27) chloroform molecules per WSe_2 unit cell. The calculated Bader charge transfer could be increased by up to a factor of four due to substrate interactions[61], which would further enhance the predicted efficiency of hole doping due to chloroform adsorption.

According to the atom-resolved projected density of states (pDOS), the chloroform orbitals are located more than 1 eV below the valence band edge or above the conduction band edge of monolayer WSe_2, and the chloroform molecule does not introduce electronic states near the band extrema or in the band gap (Fig. 3e and Supplementary Fig. 6). This suggests that the charge transfer between chloroform and WSe_2 occurs without covalent bond formation or orbital hybridization, which is consistent with the adsorption energies we calculate for the chloroform/WSe_2 system (additional states associated with chemisorption are typically accompanied by an adsorption energy < −500 meV[62]). The absence of states formed in or near the band gap suggests that chloroform doping avoids introducing scattering sites that could degrade the mobility of WSe_2.

Temporal and thermal stability of chloroform-doped WSe_2

To evaluate the long-term stability of chloroform doping, we regularly measured the charge transport characteristics of doped monolayer WSe_2 transistors for more than 8 months. Figure 4a shows the evolution of I_D vs. V_{GS} sweeps for a single doped monolayer WSe_2 device

https://doi.org/10.1038/s41467-025-65604-3

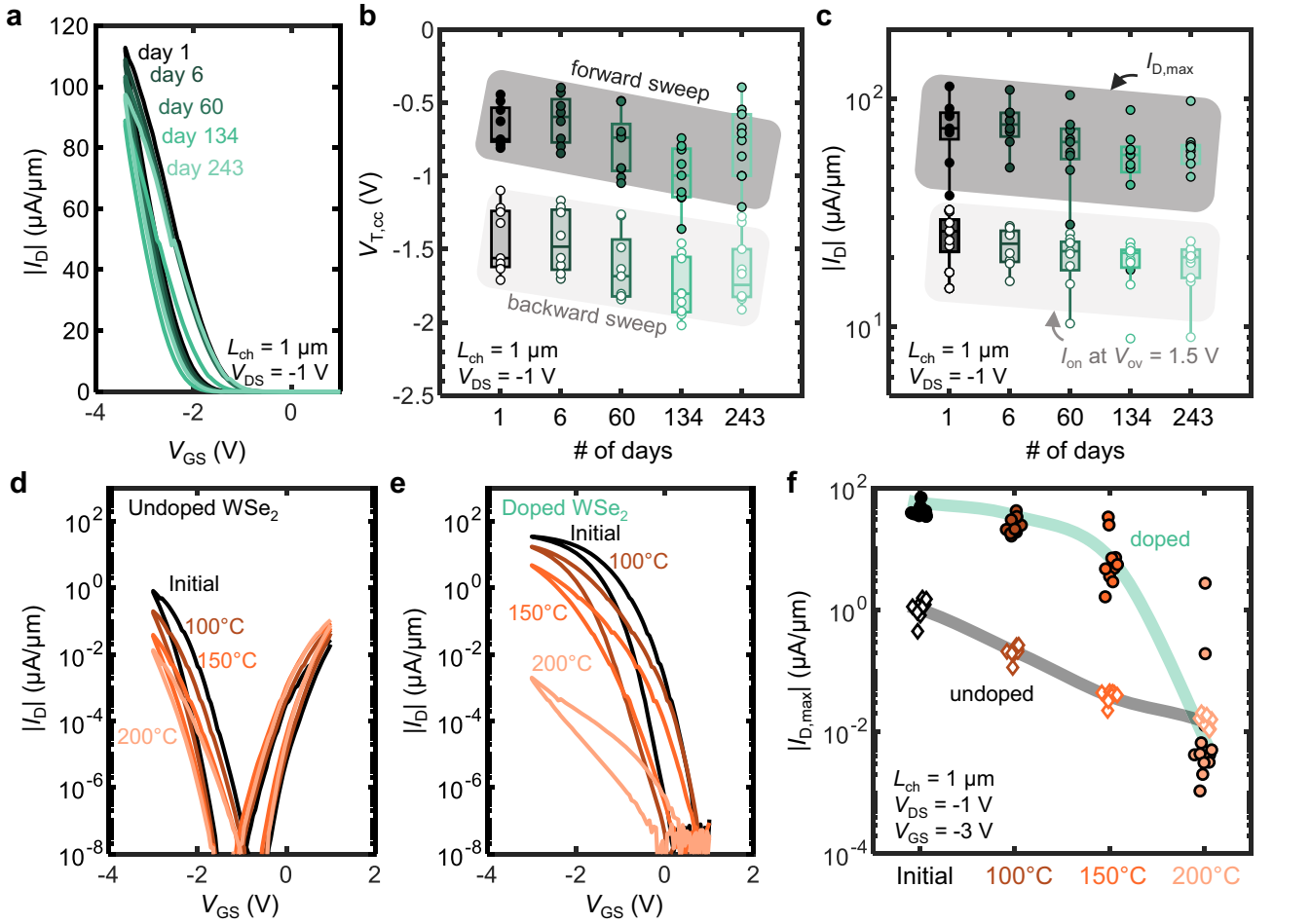

Fig. 4 | Time and temperature stability of chloroform-doped WSe_2 devices. **a** I_D vs. V_{GS} curves of a L_{ch} = 1 μm device immediately after doping and after 6, 60, 134, and 243 days. **b** Threshold voltage ($V_{T,cc}$) vs. days after doping for all L_{ch} = 1 μm devices. $V_{T,cc}$ is extracted at a constant current of 10 nA/μm at V_{DS} = −1 V for both forward and backward sweeps. **c** Drain current (both $I_{D,max}$ at V_{GS} = −3.4 V and I_{on} at V_{ov} = 1.5 V) vs. days post-doping for all L_{ch} = 1 μm devices. For panels (**b**, **c**), a box plot was created for every group of data. The central mark of the box indicates the median, and the bottom and top edges of the box indicate the 25th and 75th percentiles, respectively. **d** I_D vs. V_{GS} curves of an undoped WSe_2 device (L_{ch} = 1 μm) at V_{DS} = -1 V initially, then after annealing at 100, 150, and 200 °C. **e** I_D vs. V_{GS} curves of a doped WSe_2 device (L_{ch} = 1 μm) at V_{DS} = −1 V initially, then after annealing at 100, 150 and 200 °C. **f** $I_{D,max}$ at V_{GS} = −3.0 V after various annealing temperatures, for undoped (unfilled diamonds) and doped (filled circles) devices. For the annealing process, the devices are sequentially annealed in vacuum at ~10^{-4} Torr for 30 min at the given temperature. After annealing, the devices are cooled to room temperature for electrical measurement, then re-annealed at the next temperature.

over 243 days (>8 months). The maximum drain current $I_{D,max}$ at V_{GS} = −3.4 V, slightly decreases after 243 days from 113 μA/μm to 97.4 μA/μm. Figure 4b plots the forward and backward sweep $V_{T,cc}$ for devices with L_{ch} = 1 μm, revealing a median negative shift of −0.18 V over the course of long-term testing. This small negative shift in V_T could indicate a slight reduction in *p*-doping due to chloroform desorption.

Figure 4c summarizes the evolution of I_D in 1 μm long devices as $I_{D,max}$ for V_{GS} = -3.4 V and at V_{ov} = 1.5 V. Chloroform doping remains remarkably stable over time, with the median $I_{D,max}$ retaining >96% after 6 days and >81% after 243 days. We note that the decrease in $I_{D,max}$ can be partially attributed to the negative V_T shift because the I_{on} remains relatively stable. After 8 months, the final $I_{D,max}$ is still 76.1× higher than the initial undoped $I_{D,max}$ for the same set of devices. This demonstrates that the improved *p*-type performance from chloroform doping is highly stable over time. In contrast, other doping techniques (e.g. MoO_3[13,63], O_3 oxidation[64]) degrade rapidly in air, losing functionality over the course of several hours or days. The next-best reported example, nitric oxide, maintained performance after 24 days[25]. Additionally, the low R_C from chloroform doping was maintained after 8 months (Supplementary Fig. 7). This stability of chloroform doping over time is consistent with the strong physisorption predicted from our DFT simulations (Fig. 3c, d).

Thermal stability is also critical to enable further processing. We examined the thermal stability of undoped and chloroform-doped WSe_2 transistors by sequentially annealing them in vacuum for 30 min at 100 °C, 150 °C, and 200 °C. Figure 4d shows the I_D vs. V_{GS} of a control device, displaying a progressive decrease in hole current after each annealing step. This decline may result from the desorption of weakly-bound water molecules, which also contribute to *p*-doping[65,66]. Figure 4e plots the I_D vs. V_{GS} evolutions for a chloroform-doped device after the same annealing sequence. Similar to the undoped control device, the doped device exhibited a slight reduction in hole current after annealing at 100 °C and 150 °C. However, after the 200 °C anneal, the $I_{D,max}$ of the doped device dropped significantly to 3×10^{-3} μA/μm, comparable to the control device under similar annealing conditions. This suggests that chloroform desorbs at elevated temperatures, reverting the device to an undoped state. This is supported by activation energy calculations (Fig. 3d), which show that there is no additional barrier to desorption, leading to much faster desorption at higher temperatures.

https://doi.org/10.1038/s41467-025-65604-3

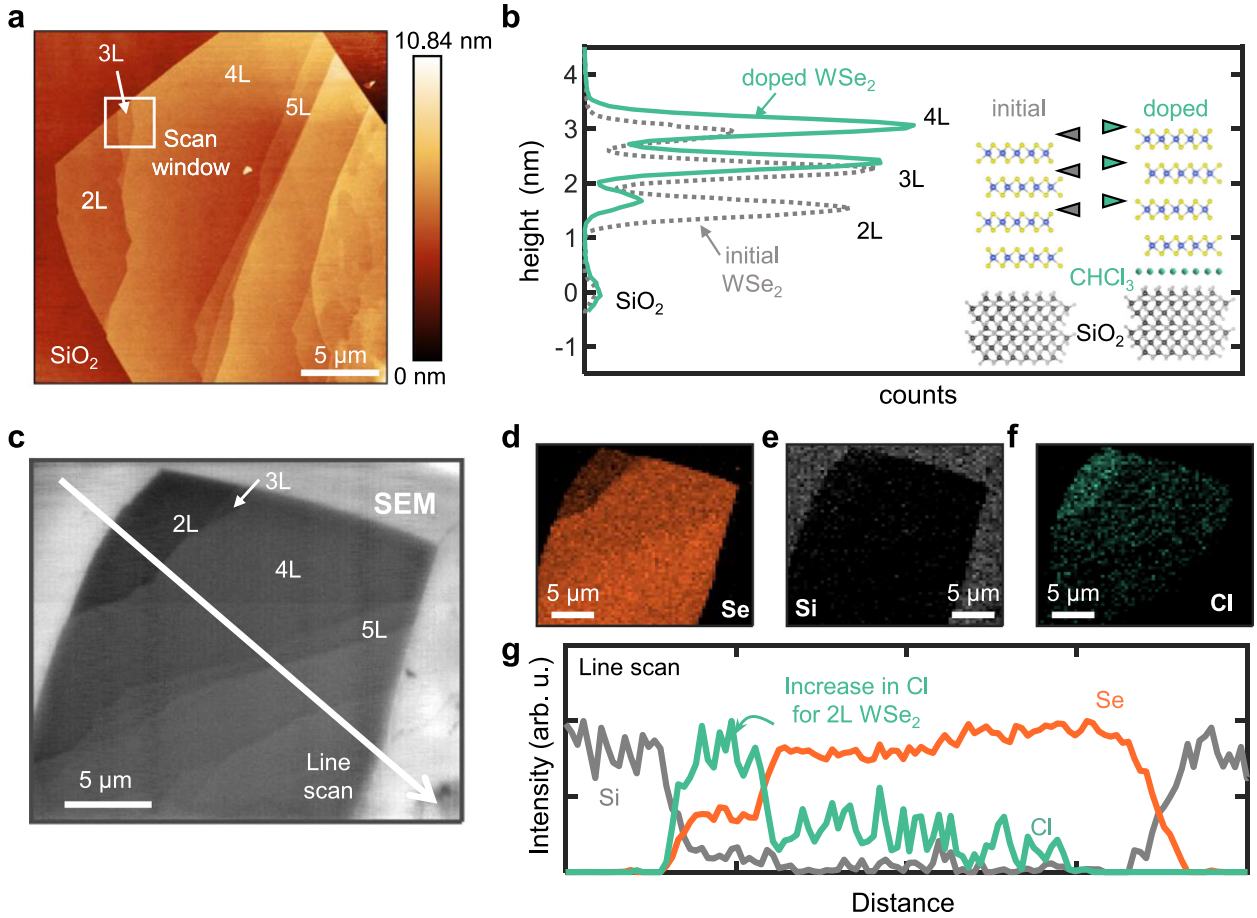

Fig. 5 | Determination of chloroform location in a WSe_2/oxide stack. a Atomic-force microscopy (AFM) of an exfoliated WSe_2 flake with various layer thicknesses. L denotes the number of WSe_2 layers. **b** Height distribution of the exfoliated flake before (gray) and after (green) doping, in the 2–4L region (as marked in panel (**a**). The peaks mark the height of the SiO_2, 2L, 3L, and 4L WSe_2 regions. There is no noticeable change in spacing between WSe_2 layers, but the difference between SiO_2 and 2L WSe_2 increases. Inset: schematic of chloroform inserting at the SiO_2/WSe_2 interface, causing an increase in height of the WSe_2 layer relative to SiO_2. Triangles denote the height of the 2L, 3L, and 4L WSe_2 regions, matching the peaks in the height distribution. **c** Scanning electron microscope (SEM) image of the exfoliated WSe_2 flake as seen in panel (**a**). **d**–**f** Elemental mapping by Auger electron spectroscopy (AES) of a doped WSe_2 flake of Se, Si, and Cl, respectively. The brighter pixels correspond to regions with higher elemental content. **g** Line scan of elemental Se, Si, and Cl content extracted from panel (**d**), showing an increase in Cl signal in the 2L WSe_2 region.

A summary of $I_{D,max}$ across all annealing stages (i.e., the initial state and anneals at 100 °C, 150 °C, and 200 °C) shows that the doped devices remain >140× higher in $I_{D,max}$ after annealing at 100 °C and 150 °C (Fig. 4f and Supplementary Fig. 8). However, following the 200 °C anneal, there was a sharp drop in hole current of the doped devices, consistent with the desorption of chloroform and a reversal to the undoped state. This sequential annealing procedure suggests that 150 °C can be treated as a safe upper-bound for the thermal stability of chloroform doping on WSe_2, although faster thermal ramping and cooling may reveal a thermal budget for higher temperatures. While this thermal budget could be a concern for direct-current (DC) operation with significant self-heating[67,68], devices operating under high frequencies will heat up less. This is because the device switching speed is higher than the 2D device thermal time constant (typically from 30 to 300 ns[69]). In any case, this 150 °C thermal budget for chloroform stability enables compatibility with oxide encapsulation by atomic-layer deposition (ALD), which often occurs between 100 and 200 °C. This may also further enhance the thermal stability of the *p*-type doping, enable fabrication of top-gated devices, and allow for concurrent application of other doping techniques, such as solid charge transfer layers (e.g., MoO_x, WO_x).

Determination of chloroform location in a WSe_2/oxide stack

To clarify the mechanism and stability of chloroform doping, we investigated its location relative to the WSe_2. Figure 5a presents a $20 \times 20\ \mu m^2$ atomic-force microscopy (AFM) topography image of an exfoliated WSe_2 flake in which the thickness increases from 2 to over 10 layers. The bilayer (2L) to four-layer (4L) region was measured in $2 \times 2\ \mu m^2$ scans before and after doping (Supplementary Fig. 9), yielding the height distributions shown in Fig. 5b. The peaks mark the height of the SiO_2, 2L, 3L, and 4L WSe_2 regions. There is no noticeable change in spacing between the WSe_2 layers, but the height difference between the SiO_2 and 2L WSe_2 increases by >0.15 nm. This suggests that chloroform does not intercalate between the WSe_2 layers, but rather that chloroform either (i) inserts at the SiO_2/WSe_2 interface, or (ii) adsorbs on top of every WSe_2 layer. X-ray diffraction (XRD) reveals that the interplanar spacing remained constant at 0.645 nm after doping (Supplementary Fig. 10), supporting the conclusion that chloroform does not intercalate between WSe_2 layers.

We measured the dependence of chloroform adsorption on WSe_2 thickness using Auger electron spectroscopy (AES). Figure 5c shows a scanning electron microscopy (SEM) image of the exfoliated WSe_2 flake from Fig. 5a, while Fig. 5d–f display AES elemental maps of Se, Si, and Cl. Figure 5g plots the AES signal intensities along the line in Fig. 5c. As a surface sensitive technique with an Auger electron escape depth of approximately 5 to 50 Å, AES confirms that the Se signal intensity scales with the WSe_2 thickness (Fig. 5d). In contrast, the Cl signal is negligible outside the WSe_2 region, peaks within the

2L WSe_2 terrace, and diminishes significantly for thicker WSe_2 layers (Fig. 5f, g).

AFM height mapping indicates uniform increases in height across the 2L, 3L, and 4L WSe_2 regions after chloroform exposure (Fig. 5b), while AES mapping shows the highest Cl signal in the (thinnest) 2L region (Fig. 5f, g). This suggests that chloroform intercalates at the WSe_2/oxide interface, as reported for graphene on SiO_2[33], with thicker WSe_2 regions attenuating the AES signals from Cl beneath the WSe_2. This interfacial chloroform may enhance the WSe_2 device performance by increasing the oxide/WSe_2 separation and reducing the influence of interfacial oxide *n*-doping[70] and trap states—which may contribute to the observed reduction in SS for doped WSe_2 devices (Fig. 2f). Although this data set is convincing, further experimental work is required to definitively confirm the intercalation of chloroform. Notably, the correlation between the Cl signal and WSe_2 regions suggests that WSe_2 is necessary for chloroform adsorption (Fig. 5f). XPS is consistent with this observation, detecting a Cl peak only in substrate regions covered by monolayer WSe_2 (Supplementary Fig. 11). In contrast, there is no apparent Cl peak in the bare substrate regions of chloroform-soaked samples.

We further assess the substrate dependence of our doping strategy and its implications for CMOS compatibility. While chloroform doping demonstrates reproducible *p*-type doping without leaving metallic residues on the surface, the sensitivity to standard wet-processing solvents (e.g., acetone) poses integration challenges (Supplementary Fig. 12a). Additionally, selective-area doping requires the development of protective strategies, such as encapsulation, that prevent dopant desorption (Supplementary Fig. 12b, c). Further experimental work is needed to optimize encapsulation strategies for localized doping. To further clarify the influence of the substrate, we extend our experiments to include WSe_2 devices on SiO_2 (Supplementary Fig. 13). These show comparable performance enhancement as those on HfO_2 (~100× increase of I_D, positive V_T shift, and similar change in carrier concentration). This suggests that the doping mechanism is robust across different amorphous dielectrics.

Overall, this work presents a straightforward and stable *p*-doping method to achieve high-performance monolayer WSe_2 transistors, while providing new mechanistic insights into solvent-based doping techniques. By achieving significant improvements in hole current, R_C, and device stability, this method offers a viable path for future low-power 2D semiconductor applications.

Methods

Doping process

The WSe_2 sample was immersed in as-purchased undiluted chloroform (SIGMA-Aldrich, No. 650498), in a watchglass-covered borosilicate beaker at standard room temperature (20-24 °C) and relative humidity (approx. 25%-65%) in a ventilated fume hood. The chloroform solvent was used without modification (as-purchased ≥99.9% chloroform). Unless indicated otherwise, the doping process occurred overnight (>8 h). Samples were exposed only to pure chloroform, as dilution with other solvents (e.g., acetone, IPA) could introduce co-dopant effects, complicating the interpretation of concentration-dependent trends. For device measurements, the doping process was performed after the initial device fabrication process was completed.

Material characterization

Raman measurements were taken on the Horiba Labram HR Evolution Raman system in the Stanford Nanofabrication Shared Facility, using 532 nm laser excitation at 1% nominal laser power (120 μW) and a spot size <1 μm in diameter. These parameters were selected to ensure minimal sample heating during measurement. For Raman and PL, a solid-source chemical vapor deposition (CVD) monolayer of WSe_2 grown on sapphire was transferred onto 100 nm SiO_2 before measurement. XPS was carried out using a PHI VersaProbe 4, equipped with a monochromatized Al Kα source (1486 eV) with a beam power of 50 W and beam energy of 15 kV, base pressure of 1.2×10^{-7} Pa, and pass energy of 224 eV (step size: 0.8 eV) and 55 eV (step size: 0.1 eV) for survey and high-resolution acquisitions, respectively.

Bulk WSe_2 crystals were exfoliated with scotch tape onto oxygen-plasma cleaned silicon wafers with 100 nm thermal oxide. The exfoliated WSe_2 was probed for Auger electron spectroscopy (AES), X-ray diffraction (XRD), and atomic-force microscopy (AFM) images in Fig. 5a and Supplementary Fig. 9. AES mapping, composition analysis, and line scans on exfoliated WSe_2 were performed on a PHI 700 Scanning Auger Nanoprobe. XRD measurements were conducted using a PANalytic Empyrean system with a Cu-Kα source. Exfoliated WSe_2 flakes were probed with symmetric 2θ/ω scans. AFM was conducted on both the exfoliated WSe_2 and on CVD-grown WSe_2 on sapphire using a Bruker Dimension Icon in peak force mode with an NSC19 Al BS probe (nominal spring constant = 0.5 N/m).

Local back-gate device fabrication on HfO_2 and electrical measurements

Continuous 2-inch CVD-grown monolayer WSe_2 on sapphire was purchased from 2D semiconductors and transferred onto local back gates of 5.3 nm HfO_2 with $C_{ox} = 2.8$ μF/cm^2. The local back gates were defined by lift-off 2 nm/8 nm Ti/Pt followed by the HfO_2 gate dielectric by thermal atomic-layer deposition at 200 °C. Coarse contact pads were then defined by lift-off 2/20 nm Ti/Pt. Polystyrene (PS) was spin-coated on top of the WSe_2 and then transferred in DI water. An O_2 plasma treatment (100 W, 1 min) of the HfO_2 dielectric was done before transferring the PS/WSe_2 film to modify the substrate's surface energy. The PS was then removed in toluene. Channel definition was done using electron-beam lithography and etched by XeF_2 (2.5 T, 30 s, 3 cycles) to define a channel width of 1 μm. Electron-beam lithography was used to pattern the fine contacts. Pd/Au (20/20 nm) was e-beam evaporated at ~10^{-8} Torr. Electrical measurements were performed at 296 K in a Janis ST-100 vacuum probe station at ~10^{-4} Torr, using a Keithley 4200 semiconductor parameter analyzer.

Cryogenic measurements were conducted in a Lakeshore cryoprobe station at ~10^{-6} Torr, using a Keithley 4200 semiconductor parameter analyzer. The sample was slowly cooled and left to stabilize overnight at 10 K before electrical testing.

For contact resistance (R_C) extraction, a pseudo-transfer length method (TLM) was used, as devices made were single devices with varying channel lengths. In this method, all devices at a certain channel length were used for R_C extraction. The total resistance in kΩ·μm (normalized by the channel width) can be expressed as $R_{TOT} = 2R_C + R_{ch} = 2R_C + R_{sh}L_{ch}$, where R_{sh} is the sheet resistance of the channel and R_{ch} is the channel resistance. R_C is evaluated by plotting R_{TOT} versus L_{ch} and drawing a linear fit through *all* data points, and the *y*-intercept at $L_{ch} = 0$ gives $2R_C$. The R_C is extracted for each gate overdrive $V_{ov} = |V_{GS} - V_T|$, with V_T from the constant-current method at $I_D = 10^{-2}$ μA/μm.

Low temperature photoluminescence

Low-temperature photoluminescence spectroscopy was conducted with a 532 nm excitation laser, ~1 μm spot size, and 600 l/mm spectrometer grating. The laser power was fixed at 60 μW, unless otherwise noted. The emission was collected using a 50× objective with a numerical aperture of 0.55, with 2 s acquisition times and 2 accumulations. The sample was cooled to a base temperature of ~6.7 K, then warmed up using a resistive heater for temperature-dependent measurements. For temperature-dependent experiments, the sample sat for 30 min at the desired temperature to stabilize before collecting the spectra. For this experiment, CVD-grown WSe_2 was wet transferred (as described above) onto 100 nm SiO_2/p^{++} Si, then half of

the chip was cleaved and subjected to an overnight chloroform soak. Several spots across both the control and doped samples were examined to ensure peak shape consistency. Finally, peak fitting was conducted in Origin using a Gaussian-Lorentzian blend.

Temporal and thermal stability testing

For time stability measurements, devices were stored at room temperature in a nitrogen dry box under continuous N_2 purge, with relative humidity maintained at ~5%. For thermal stability testing, initial electrical measurements were performed at 296 K in a Janis ST-100 vacuum probe station at $\sim 10^{-4}$ Torr, using a Keithley 4200 semiconductor parameter analyzer. The samples were then in-situ annealed at 100 °C, held for 30 min, then left to cool down for >5 h. Electrical measurements were taken at 300 K in a vacuum. This process was then repeated at 150 °C and 200 °C, respectively, with device measurements in between, without breaking the vacuum. At present, the impact of ambient humidity and oxygen on the long-term stability of chloroform doping remains an open question and warrants future investigation, particularly in the context of encapsulated or integrated device architectures.

Density functional theory (DFT) simulations

First, a variable cell relaxation was performed to optimize the lattice coordinates within the monolayer WSe_2 primitive cell. The optimized primitive cell was then scaled to a 5×5 supercell, interfaced with a chloroform molecule, and then subjected to a fixed cell relaxation to determine the WSe_2/chloroform atomic coordinates. Both the Cl-facing and H-facing orientations were considered, where the chlorine or hydrogen atom of the chloroform molecule was oriented towards the WSe_2. Quantum ESPRESSO 7.1[71] was used for all DFT simulations, and the van der Waals interactions between the chloroform and WSe_2 monolayer were modeled using the vdW-DF-C09 correction. For all self-consistent calculations, we use Γ-point sampling for all 5×5 supercells, and k-point grids of $3 \times 3 \times 1$ and $7 \times 7 \times 1$ for the 3×3 and 2×2 supercells, respectively. We perform non-self-consistent calculations on a $15 \times 15 \times 1$ k-point grid prior to extracting the density of states for the WSe_2 + chloroform assemblies. All DFT calculations use projector-augmented wave pseudopotentials with kinetic energy cutoffs and charge density cutoffs of 50 and 400 Ry, respectively. We use the "Bader" code[72] for Bader charge analysis, PyProcar[73] for plotting projected density of states and band structures, and VESTA[74] for plotting isosurfaces. We note that in this work, we consider only interactions between the chloroform and WSe_2 without an insulator or substrate. Including the amorphous SiO_2 and HfO_2 would improve the accuracy of our simulations by capturing chloroform-substrate interactions; however, simulating this interface is computationally demanding, and we leave it as a promising research direction.

Other orientations of chloroform on WSe_2 are certainly possible, although a rigorous test for the most favorable orientation remains outside of the scope of this study. We confirmed that the Cl-facing orientation is stable compared to other similar random orientations by rotating the chloroform molecule by 5 degrees (i.e., tilting the C-H bond 5 degrees relative to the surface normal) and then re-relaxing the system. The chloroform molecule returned close to its original position and total energy (to within 2 meV), suggesting that this orientation is indeed favorable.

Data availability

Relevant data supporting the key findings of this study are available within the article and the Supplementary Information file. All raw data generated during the current study are available from the corresponding authors upon request.

References

1. O'Brien, K. P. et al. Process integration and future outlook of 2D transistors. *Nat. Commun.* **14**, 6400 (2023).
2. Kim, K. S. et al. The future of two-dimensional semiconductors beyond Moore's law. *Nat. Nanotechnol.* **19**, 895–906 (2024).
3. Razavieh, A., Zeitzoff, P. & Nowak, E. J. Challenges and limitations of CMOS Scaling for FinFET and beyond architectures. *IEEE Trans. Nanotechnol.* **18**, 999–1004 (2019).
4. Shen, P.-C. et al. Ultralow contact resistance between semimetal and monolayer semiconductors. *Nature* **593**, 211–217 (2021).
5. Li, W. et al. Approaching the quantum limit in two-dimensional semiconductor contacts. *Nature* **613**, 274–279 (2023).
6. Allain, A., Kang, J., Banerjee, K. & Kis, A. Electrical contacts to two-dimensional semiconductors. *Nat. Mater.* **14**, 1195–1205 (2015).
7. Liu, Y. et al. Low-resistance metal contacts to encapsulated semiconductor monolayers with long transfer length. *Nat. Electron.* **5**, 579–585 (2022).
8. Lin, Y.-T. et al. Antimony–platinum modulated contact enabling majority carrier polarity selection on a monolayer tungsten diselenide channel. *Nano Lett.* **24**, 8880–8886 (2024).
9. Hoang, L. et al. Enabling P-type conduction in bilayer WS_2 with NbP topological semimetal contacts. Preprint at http://arxiv.org/abs/2409.18926 (2024).
10. Kozhakhmetov, A. et al. Controllable p-type doping of 2D WSe_2 via vanadium substitution. *Adv. Funct. Mater.* **31**, 2105252 (2021).
11. Qin, Z. et al. Growth of Nb-doped monolayer WS_2 by liquid-phase precursor mixing. *ACS Nano* **13**, 10768–10775 (2019).
12. Kanahashi, K. et al. Dimensionality-induced transition from degenerate to nondegenerate states in Nb-doped WSe_2. *ACS Nano* **19**, 10244–10254 (2025).
13. Cai, L. et al. Rapid flame synthesis of atomically thin MoO_3 down to monolayer thickness for effective hole doping of WSe_2. *Nano Lett.* **17**, 3854–3861 (2017).
14. Pang, C. S. et al. Atomically controlled tunable doping in high-performance WSe_2 devices. *Adv. Electron. Mater.* **6**, 1901304 (2020).
15. Lin, Y.-T. et al. Photolithography-induced doping and interface modulation for high-performance monolayer WSe_2 P-type transistors. *Nano Lett.* **25**, 3571–3578 (2025).
16. Kim, I. et al. Low contact resistance WSe_2 *p*-type transistors with highly stable, CMOS-compatible dopants. *Nano Lett.* **24**, 13528–13533 (2024).
17. Hung, T. Y. T. et al. pMOSFET with CVD-grown 2D semiconductor channel enabled by ultra-thin and fab-compatible spacer doping. In *2022 International Electron Devices Meeting (IEDM)*. Vol. 2022 7.3.1–7.3.4 (IEEE, 2022).
18. Oberoi, A. et al. Toward high-performance p-type two-dimensional field effect transistors: contact engineering, scaling, and doping. *ACS Nano* **17**, 19709–19723 (2023).
19. Chiang, C.-C. et al. Air-stable P-doping in record high-performance monolayer WSe_2 devices. *IEEE Electron Device Lett.* **43**, 319 (2022).
20. Fang, H. et al. High-performance single layered WSe_2 p-FETs with chemically doped contacts. *Nano Lett.* **12**, 3788–3792 (2012).
21. Ho, P. H. et al. High-performance WSe_2 top-gate devices with strong spacer doping. *Nano Lett.* **23**, 10236–10242 (2023).
22. Choi, M. S. et al. Lateral MoS_2 p-n junction formed by chemical doping for use in high-performance optoelectronics. *ACS Nano* **8**, 9332–9340 (2014).
23. Xie, J. et al. Low resistance contact to P-type monolayer WSe_2. *Nano Lett.* **24**, 5937–5943 (2024).
24. Pack, J. et al. Charge-transfer contacts for the measurement of correlated states in high-mobility WSe_2. *Nat. Nanotechnol.* **19**, 948–954 (2024).

25. Lan, H.-Y. et al. Uncovering the doping mechanism of nitric oxide in high-performance P-type WSe_2 transistors. *Nat. Commun.* **16**, 4160 (2025).
26. Ghosh, S. et al. High-performance p-type bilayer WSe_2 field effect transistors by nitric oxide doping. *Nat. Commun.* **16**, 5649 (2025).
27. Lee, D. et al. Remote modulation doping in van der Waals heterostructure transistors. *Nat. Electron.* **4**, 664–670 (2021).
28. Wang, Y., Sarkar, S., Yan, H. & Chhowalla, M. Critical challenges in the development of electronics based on two-dimensional transition metal dichalcogenides. *Nat. Electron.* **7**, 638–645 (2024).
29. Yang, L. et al. Chloride molecular doping technique on 2D materials: WS_2 and MoS_2. *Nano Lett.* **14**, 6275–6280 (2014).
30. Devi, D. S. & Mohapatra, N. R. Exploring *p*-type contact for monolayer WS_2 FETs using Halogen Doping and Intermediate Layers. *ACS Omega* **9**, 50634–50641 (2024).
31. Zhang, H. et al. Improvement of P-type contact in WSe_2 field-effect transistors via defect engineering. *Nano Lett.* **25**, 2803–2809 (2025).
32. Zou, T. et al. High-performance solution-processed 2D P-type WSe_2 transistors and circuits through molecular doping. *Adv. Mater.* **35**, e2208934 (2023).
33. Kim, H. H. et al. Substrate-induced solvent intercalation for stable graphene doping. *ACS Nano* **7**, 1155–1162 (2013).
34. Choi, J., Zhang, H., Du, H. & Choi, J. H. Understanding solvent effects on the properties of two-dimensional transition metal dichalcogenides. *ACS Appl. Mater. Interfaces* **8**, 8864–8869 (2016).
35. Poddar, P. K. et al. Resist-free lithography for monolayer transition metal dichalcogenides. *Nano Lett.* **22**, 726–732 (2022).
36. Chou, A.-S. et al. High-performance monolayer WSe_2 p/n FETs via antimony-platinum modulated contact technology towards 2D CMOS Electronics. In *2022 International Electron Devices Meeting (IEDM)* 7.2.1–7.2.4 (IEEE, 2022).
37. O'Brien, K. P. et al. Advancing 2D monolayer CMOS through contact, channel and interface engineering. In *2021 IEEE International Electron Devices Meeting (IEDM)* 7.1.1-7.1.4 (IEEE, 2021).
38. Maxey, K. et al. 300 mm MOCVD 2D CMOS materials for more (than) Moore scaling. In *2022 IEEE Symposium on VLSI Technology and Circuits (VLSI Technology and Circuits)* 419–420 (IEEE, 2022).
39. Lan, H.-Y., Tripathi, R., Liu, X., Appenzeller, J. & Chen, Z. Wafer-scale CVD monolayer WSe_2 p-FETs with Record-high 727 μA/μm I_{on} and 490 μS/μm g_{max} via hybrid charge transfer and molecular doping. In *2023 International Electron Devices Meeting (IEDM)* 1–4 (IEEE, 2023).
40. Chou, A.-S. et al. Status and performance of integration modules toward scaled CMOS with transition metal dichalcogenide channel. In *2023 International Electron Devices Meeting (IEDM)* 1–4 (IEEE, 2023).
41. Ortiz-Conde, A. et al. A review of recent MOSFET threshold voltage extraction methods. *Microelectron. Reliab.* **42**, 583–596 (2002).
42. Lockhart De La Rosa, C. J. et al. Highly efficient and stable MoS_2 FETs with reversible n-doping using a dehydrated poly(vinyl-alcohol) coating. *Nanoscale* **9**, 258–265 (2017).
43. Ber, E., Grady, R. W., Pop, E. & Yalon, E. Uncovering the different components of contact resistance to atomically thin semiconductors. *Adv. Electron. Mater.* **9**, 2201342 (2023).
44. Baikadi, P., Vandenberghe, W., Reyntjens, P., Kim, R. & Van de Put, M. Quantum transport study of transition-metal dichalcogenide top-contacted geometries investigating the impact of nonuniform doping, dielectric environment, and image-force barrier lowering. *Phys. Rev. Appl.* **22**, 064058 (2024).
45. Illarionov, Y. Y. et al. Insulators for 2D nanoelectronics: the gap to bridge. *Nat. Commun.* **11**, 3385 (2020).
46. Liu, M. et al. Periodical Ripening for MOCVD Growth of Large 2D Transition Metal Dichalcogenide Domains. *Adv. Funct. Mater.* **33**, 2212773 (2023).
47. Lyons, T. P. et al. The valley Zeeman effect in inter- and intra-valley trions in monolayer WSe_2. *Nat. Commun.* **10**, 2330 (2019).
48. Jadczak, J. et al. Probing of free and localized excitons and trions in atomically thin WSe_2, WS_2, $MoSe_2$ and MoS_2 in photoluminescence and reflectivity experiments. *Nanotechnology* **28**, 395702 (2017).
49. Wu, Z. et al. Defects as a factor limiting carrier mobility in WSe_2: a spectroscopic investigation. *Nano Res* **9**, 3622–3631 (2016).
50. Wu, Z. et al. Defect activated photoluminescence in WSe_2 monolayer. *J. Phys. Chem. C.* **121**, 12294–12299 (2017).
51. Greben, K., Arora, S., Harats, M. G. & Bolotin, K. I. Intrinsic and extrinsic defect-related excitons in TMDCs. *Nano Lett.* **20**, 2544–2550 (2020).
52. Munson, K. T. et al. Influence of substrate-induced charge doping on defect-related excitonic emission in monolayer MoS_2. *J. Phys. Chem. Lett.* **15**, 7850–7856 (2024).
53. Amani, M. et al. Near-unity photoluminescence quantum yield in MoS_2. *Science* **350**, 1065–1068 (2015).
54. Schwarz, A. et al. Thiol-based defect healing of WSe_2 and WS_2. *npj 2D Mater. Appl.* **7**, 59 (2023).
55. Park, J. H. et al. Defect passivation of transition metal dichalcogenides via a charge transfer van der Waals interface. *Sci. Adv.* **3**, e1701661 (2017).
56. Kong, L., Enders, A., Rahman, T. S. & Dowben, P. A. Molecular adsorption on graphene. *J. Phys. Condens. Matter* **26**, 443001 (2014).
57. Zhou, C., Yang, W. & Zhu, H. Mechanism of charge transfer and its impacts on Fermi-level pinning for gas molecules adsorbed on monolayer WS_2. *J. Chem. Phys.* **142**, 214704 (2015).
58. Szary, M. J. Toward high selectivity of sensor arrays: enhanced adsorption interaction and selectivity of gas detection (N_2, O_2, NO, CO, CO_2, NO_2, SO_2, AlH_3, NH_3, and PH_3) on transition metal dichalcogenides (MoS_2, $MoSe_2$, and $MoTe_2$). *Acta Mater.* **274**, 120016 (2024).
59. Nam, T., Seo, S. & Kim, H. Atomic layer deposition of a uniform thin film on two-dimensional transition metal dichalcogenides. *J. Vac. Sci. Technol. A Vacuum Surfaces Film.* **38**, 030803 (2020).
60. Parija, A. et al. Electronic structure modulation of MoS_2 by substitutional Se incorporation and interfacial MoO_3 hybridization: Implications of Fermi engineering for electrocatalytic hydrogen evolution and oxygen evolution. *Chem. Phys. Rev.* **2**, 011401 (2021).
61. Mehmood, F. & Pachter, R. Density functional theory study of chemical sensing on surfaces of single-layer MoS_2 and graphene. *J. Appl. Phys.* **115**, 164302 (2014).
62. Paso, K. G. In *Microbial Biodegradation and Bioremediation*. 109–143 (Elsevier, 2022).
63. Xie, L. et al. Electrical measurement of non-destructively p-type doped graphene using molybdenum trioxide. *Appl. Phys. Lett.* **99**, 012112 (2011).
64. Yamamoto, M., Nakaharai, S., Ueno, K. & Tsukagoshi, K. Self-limiting oxides on WSe_2 as controlled surface acceptors and low-resistance hole contacts. *Nano Lett.* **16**, 2720–2727 (2016).
65. Ovchinnikov, D., Allain, A., Huang, Y. S., Dumcenco, D. & Kis, A. Electrical transport properties of single-layer WS_2. *ACS Nano* **8**, 8174–8181 (2014).
66. Qiu, H. et al. Electrical characterization of back-gated bi-layer MoS_2 field-effect transistors and the effect of ambient on their performances. *Appl. Phys. Lett.* **100**, 123104 (2012).
67. Wang, M. A. & Pop, E. Monte Carlo simulation of electrical transport with joule heating and strain in monolayer MoS_2 devices. *Nano Lett.* **25**, 6841–6847 (2025).

68. Yalon, E. et al. Energy dissipation in monolayer MoS_2 electronics. *Nano Lett.* **17**, 3429–3433 (2017).
69. Islam, S., Li, Z., Dorgan, V. E., Bae, M.-H. & Pop, E. Role of joule heating on current saturation and transient behavior of graphene transistors. *IEEE Electron Device Lett.* **34**, 166–168 (2013).
70. Ko, K. et al. Competition between bipolar conduction modes in extrinsically *p*-doped MoS_2: interaction with gate dielectric matters. *ACS Nano* **19**, 1630–1641 (2025).
71. Giannozzi, P. et al. Quantum ESPRESSO toward the exascale. *J. Chem. Phys.* **152**, 154105 (2020).
72. Henkelman, G., Arnaldsson, A. & Jónsson, H. A fast and robust algorithm for Bader decomposition of charge density. *Comput. Mater. Sci.* **36**, 354–360 (2006).
73. Herath, U., Tavadze, P. & He, X. PyProcar: a Python library for electronic structure pre/post-processing. *Comput. Phys. Commun.* **251**, 107080 (2020).
74. Momma, K. & Izumi, F. VESTA 3 for three-dimensional visualization of crystal, volumetric and morphology data. *J. Appl. Crystallogr.* **44**, 1272–1276 (2011).
75. Mortelmans, W. et al. Record performance in GAA 2D NMOS and PMOS using monolayer MoS_2 and WSe_2 with scaled contact and gate length. In *2024 IEEE Symposium on VLSI Technology and Circuits (VLSI Technology and Circuits)* 1–2 (IEEE, 2024).
76. Dorow, C. et al. Advancing monolayer 2-D nMOS and pMOS transistor integration from growth to Van der Waals interface engineering for ultimate CMOS scaling. *IEEE Trans. Electron Devices* **68**, 6592–6598 (2021).
77. Wang, Y. et al. P-type electrical contacts for 2D transition-metal dichalcogenides. *Nature* **610**, 61–66 (2022).
78. Kim, K. S. et al. Non-epitaxial single-crystal 2D material growth by geometric confinement. *Nature* **614**, 88–94 (2023).
79. Penumatcha, A. et al. High mobility TMD NMOS and PMOS transistors and GAA architecture for ultimate CMOS Scaling. In *2023 International Electron Devices Meeting (IEDM)* 1–4 (IEEE, 2023).
80. Wang, X., Xiong, X., Shi, X., Gu, C. & Wu, Y. Optimized electrical properties of p-type field-effect transistors based on WSe_2 grown at moderate temperatures. *Appl. Phys. Lett.* **123**, 261901 (2023).
81. Dorow, C. J. et al. Exploring manufacturability of novel 2D channel materials: 300 mm wafer-scale 2D NMOS & PMOS using MoS_2, WS_2, & WSe_2. In *2023 International Electron Devices Meeting (IEDM)* 1–4 (IEEE, 2023).

Acknowledgements

This work was supported by the National Science Foundation (NSF) FuSe2 grant 2425218 and the TSMC-Stanford SystemX Alliance. L.H. was supported by the Sandia Microelectronics: Accelerating Research Talent (SMART) Internship. L.H., R.K.A.B., T.P., and E.P. acknowledge support from SUPREME, a JUMP 2.0 center within the Semiconductor Research Corporation (SRC), sponsored by the Defense Advanced Research Projects Agency (DARPA). R.K.A.B. was supported by the Stanford Graduate Fellowship and the NSERC PGS-D programs. T.P. acknowledges support from the NSF MPS-Ascend postdoctoral fellowship. A.P.S. and F.L. were supported by the U.S. Department of Energy, Office of Science, Basic Energy Sciences, CPIMS Program, under award no. DE-SC0026181. Part of this work was performed at the Stanford Nanofabrication Facility (SNF) and Stanford Nano Shared Facilities (SNSF), supported by NSF award ECCS-2026822. The authors thank Krishna C. Saraswat, Johnathan Georgaras, Qingrui Cao, Akash Ramdas, Emily Chen, and Alex Shearer for valuable discussions.

Author contributions

L.H. fabricated the devices and conducted the device measurements and analysis under the supervision of A.J.M. and E.P. L.H. conducted the AFM, Raman, and Auger measurements. R.K.A.B. performed the DFT simulations. A.T.H. performed the CVD WSe_2 material growth. T.P. and L.H. performed the low-temperature PL characterization and analysis with the help of A.P.S. under the supervision of F.L. Z.Z. performed the XRD with L.H. M.H. performed the WSe_2 exfoliation. M.J. performed SiO_2 thermal oxidation and provided initial fabrication support. L.H. and A.J.M. wrote the paper. All authors have given approval to the final version of the manuscript.

Competing interests

The authors declare no competing interests.

Additional information

Supplementary information The online version contains supplementary material available at https://doi.org/10.1038/s41467-025-65604-3.

Correspondence and requests for materials should be addressed to Andrew J. Mannix.

Peer review information *Nature Communications* thanks Cheol-Joo Kim, who co-reviewed with Woo-Ju Lee, Soumya Sarkar, and the other anonymous reviewer for their contribution to the peer review of this work. A peer review file is available.

Supplementary Information

Low Resistance *P*-Type Contacts to Monolayer WSe_2 through Chlorinated Solvent Doping

Lauren Hoang[1], Robert K.A. Bennett[1], Anh Tuan Hoang[2], Tara Peña[1], Zhepeng Zhang[2], Marisa Hocking[2], Ashley P. Saunders[3], Marc Jaikissoon[1], Fang Liu[3], Eric Pop[1,2,4], and Andrew J. Mannix[2,*]

[1]*Dept. of Electrical Engineering, Stanford University, Stanford, CA 94305, U.S.A.*

[2]*Dept. of Materials Science and Engineering, Stanford University, Stanford, CA 94305, U.S.A.*

[3]*Dept. of Chemistry, Stanford University, Stanford, CA 94305, U.S.A.*

[4]*Dept. of Applied Physics, Stanford University, Stanford, CA 94305, U.S.A.*

This file includes

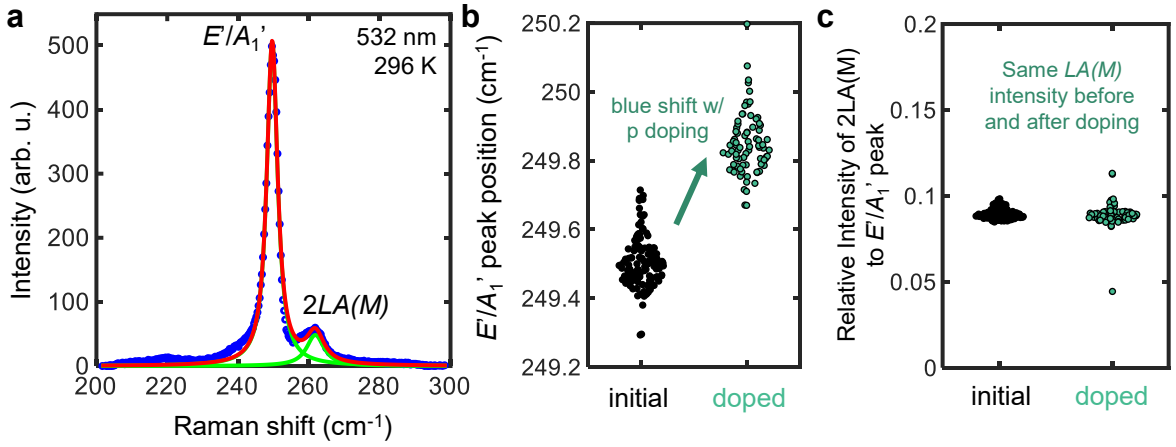

Supplementary Fig. 1 | Raman Spectroscopy on Monolayer WSe_2. a, Representative Raman spectra (blue points) and peak fitting of E'/A_1' and 2LA(M) peak using a Gaussian-Lorentzian line shape for all peaks. An iterative least-square method in MATLAB was used where the baseline of the spectra was subtracted prior to fitting. **b**, Extracted WSe_2 E'/A_1' peak position before and after chloroform doping, showing a blueshift[1–3] with doping. CVD-grown monolayer WSe_2 on SiO_2 was used for before and after doping comparison on the same WSe_2 flake. **c**, Relative intensity of the 2LA(M) peak to the E'/A_1' peak of monolayer WSe_2, showing negligible change in 2LA(M) intensity.

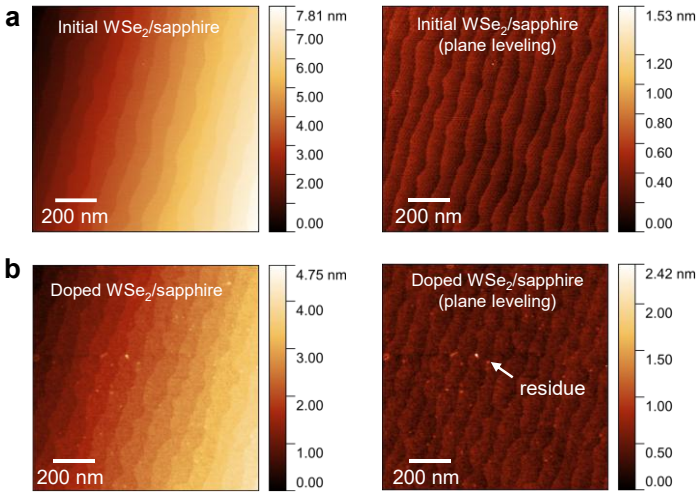

Supplementary Fig. 2 | a, Atomic Force Microscopy (AFM) image (scan size 1 × 1 μm^2) of monolayer WSe_2 grown directly on sapphire, showing low root mean square (RMS) surface roughness (RMS ~ 0.08 nm). **b**, AFM image (scan size 1 × 1 μm^2) of monolayer WSe_2 grown directly on sapphire, after doping in chloroform overnight. Some small residues can be identified on the WSe_2 flake, but there is still low surface roughness (RMS ~0.13 nm).

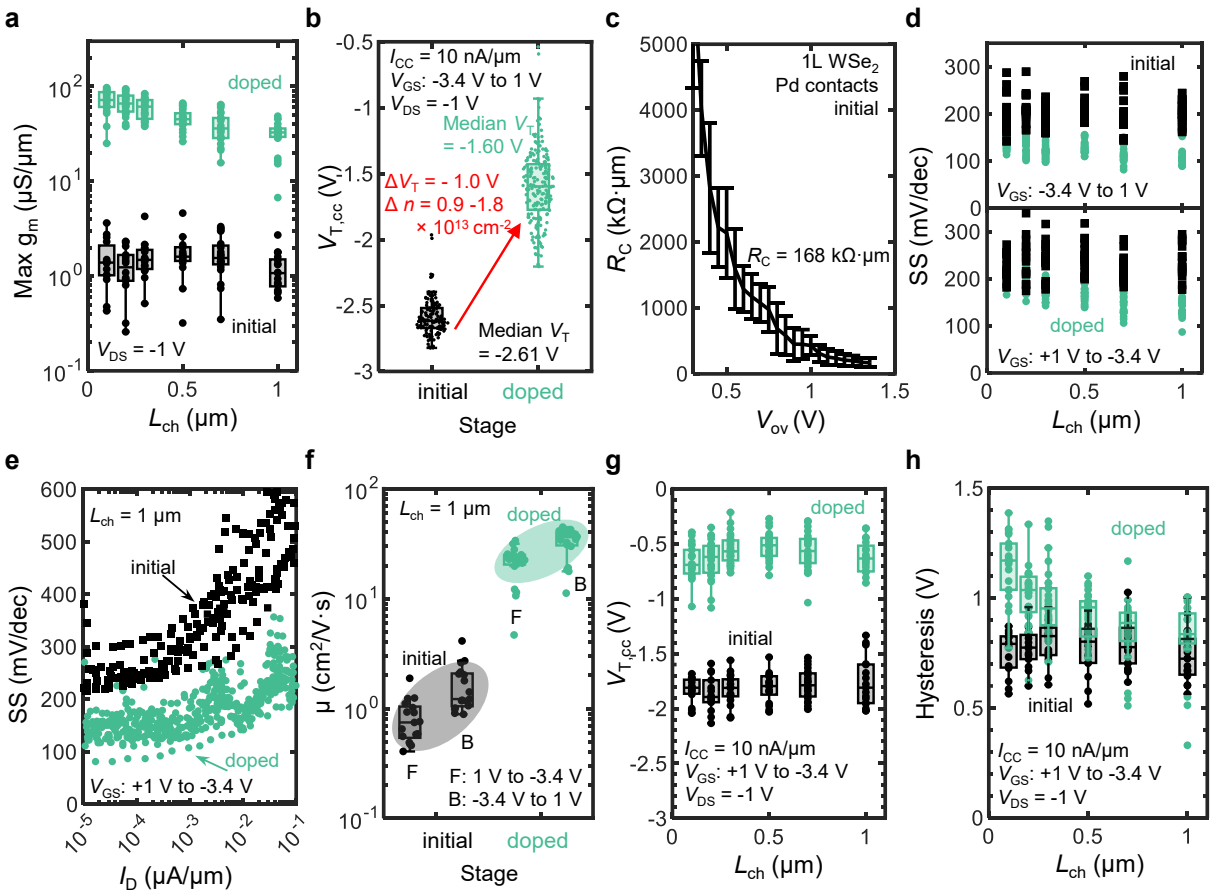

Supplementary Fig. 3 | Additional Electrical Device Analysis. a, Maximum transconductance (g_m) vs. channel length (L_{ch}) for undoped and doped devices, reaching >100 μS/μm for doped WSe_2. **b**, Constant-current threshold voltage ($V_{T,cc}$) at $I_{D,cc}$ = 10 nA/μm before and after *p*-doping. Devices show a median V_T shift of +1.0 V, corresponding to $\Delta n = C_{ox} \Delta V_T/q$ = 0.9 - 1.8 × 10^{13} cm^{-2} carriers induced (with C_{ox} = 1.38 to 2.8 μF/cm^2). **c**, Contact resistance (R_C) vs. overdrive gate voltage ($V_{ov} = |V_{GS} - V_T|$) of monolayer WSe_2 devices with Pd contacts before doping. **d**, Minimum subthreshold swing (SS) with respect to L_{ch} of doped and undoped monolayer WSe_2 devices for backward (top) and forward (bottom) V_{GS} sweep directions. **e**, SS vs. I_D in 1 μm long devices before and after doping, sweeping V_{GS} from +1 V to -3.4V (forward direction). Doped devices show lower SS for the whole sub-threshold I_D range. **f**, The mobility $\mu = g_m L_{ch}/(WC_{ox}|V_{DS}|)$ is estimated from the forward and backward V_{GS} sweeps for L_{ch} = 1 μm devices before and after doping (F and B indicate the forward and backward sweep directions, with the ranges shown in the inset). C_{ox} denotes the back-gate oxide capacitance per unit area. Mobility is extracted from long channel devices to reduce the impact of contact resistance. The initial devices are strongly contact-limited, making accurate pre-doping mobility extraction difficult. The estimated post-doping mobility is approximately 22.7 to 36.2 $cm^2/(V \cdot s)$ at V_{DS} = -1 V. **g**, $V_{T,cc}$ at $I_{D,cc}$ = 10 nA/μm before and after *p*-doping, sweeping from +1 V to -3.4 V. **Figure 2d** shows the counterpart $V_{T,cc}$ for the backward sweep direction from -3.4 V to 1V. **h**, Hysteresis at I_D = 10 nA/μm with respect to L_{ch}, for both undoped and doped devices. For panels a, b, f-h, a box plot was created for every group of data. The central mark of the box indicates the median, and the bottom and top edges of the box indicate the 25th and 75th percentiles, respectively.

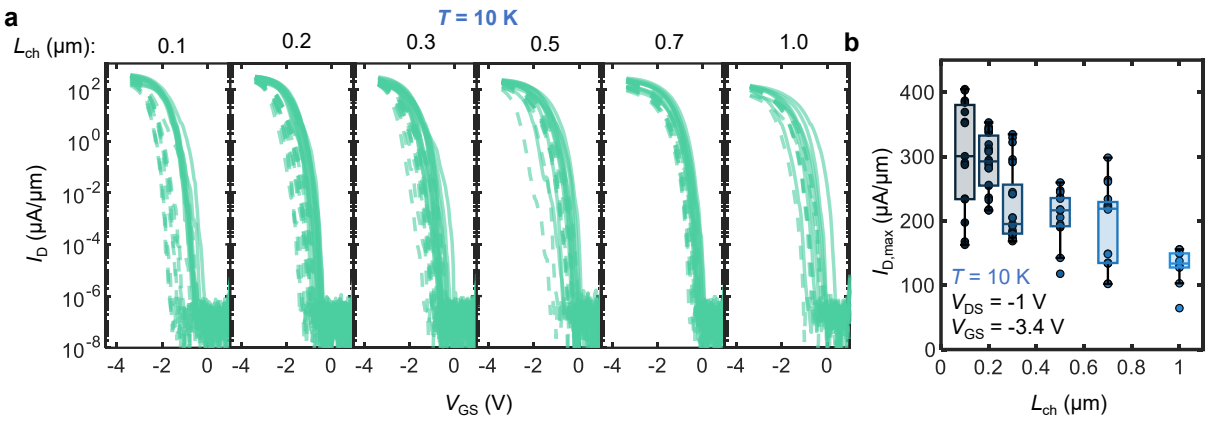

Supplementary Fig. 4 | Low Temperature Electrical Measurements of Chloroform-doped Monolayer WSe_2 Transistors. **a**, Measured I_D vs. V_{GS} at 10 K after doping for various channel length (L_{ch} = 0.1 to 1.0 μm) devices. Solid (dashed) lines indicate V_{GS} sweeps from positive (negative) to negative (positive) gate bias. **b**, Maximum drain-current $I_{D,max}$ at V_{GS} = - 3.4 V at 10 K as a function of L_{ch}. An $I_{D,max}$ of 403 μA/μm was achieved for a L_{ch} = 0.1 μm device. A box plot was created for every group of data. The central mark of the box indicates the median, and the bottom and top edges of the box indicate the 25th and 75th percentiles, respectively.

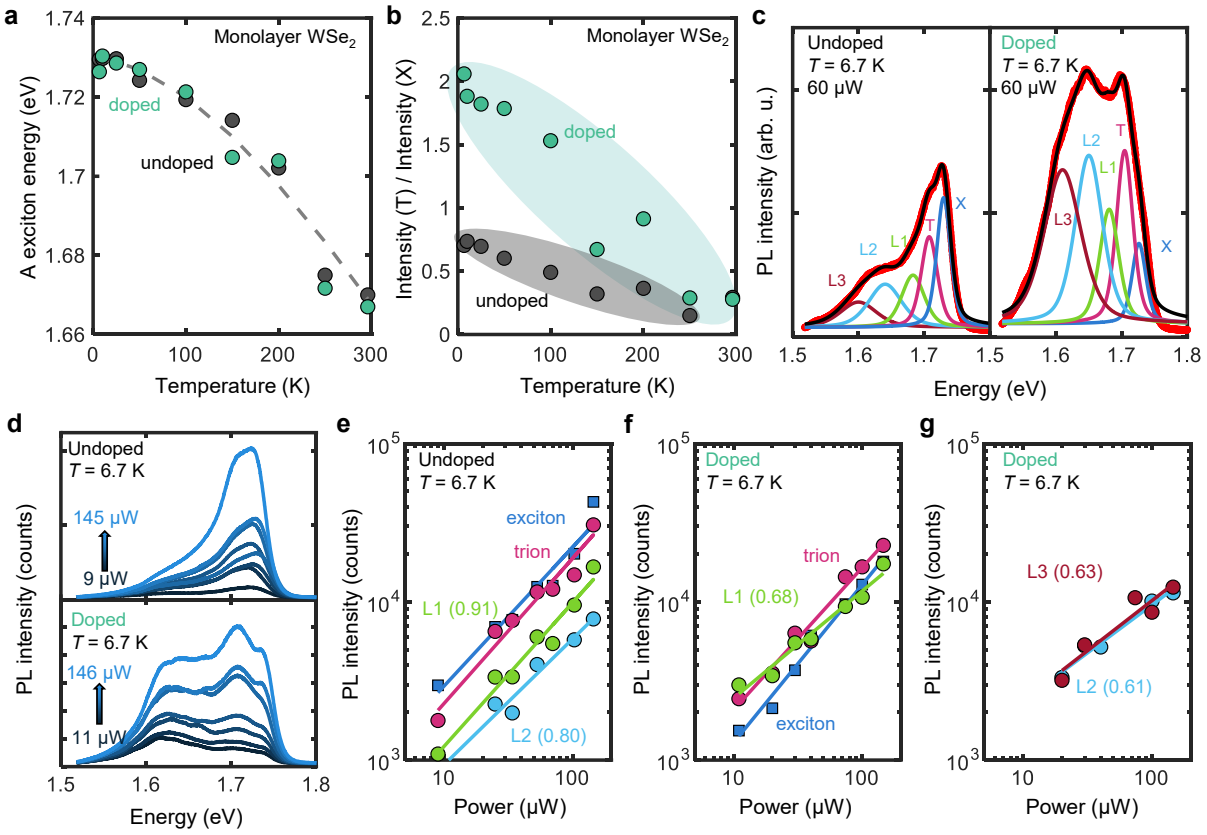

Supplementary Fig. 5 | Temperature-dependent Photoluminescence Spectroscopy. **a**, Neutral A exciton (X) energy as a function of temperature for both undoped and doped WSe_2. The exciton peak redshifts with increasing temperature, consistent with the expected band gap reduction described by the Varshni equation[4]. The data is fitted to the Varshni equation and displayed with a dashed line. **b**, Relative intensity of the trion peak to the exciton peak at different temperatures for undoped and doped WSe_2. The doped sample shows consistently higher trion intensity compared to the undoped sample. **c**, PL spectra and peak fitting of 5 peaks (X, T, L1, L2, L3) of an undoped (left) and doped (right) spectra. Noticeably, the exciton (X) intensity is higher than the trion (T), L1, L2, and L3 in the undoped sample, but lower in the doped sample. **d**, PL spectra under different laser powers collected at 6.7 K for an undoped (top) and doped (bottom) WSe_2 sample, respectively. **e**, PL intensity vs. laser power for the X, T, L1, and L2 peaks for undoped WSe_2. **f**, PL intensity vs. laser power for the X, T, and L1 peaks of doped WSe_2. The trion intensity is higher than the exciton intensity for doped WSe_2. **g**, PL intensity vs. laser power of L2 and L3 peaks of doped WSe_2. For panels e-g, the number in parenthesis indicates the power dependence (α) by fitting a power law $I \propto P^{\alpha}$ to the data, where I is the PL peak intensity for a given laser power, P. The two higher energy peaks (X, T) for both samples have near-linear fit of the peak intensity with laser power (α ~ 1), which is consistent with the exciton and trion behavior and is attributed to radiative recombination of excitons and trions. In comparison, peaks L1 - L3 exhibit sublinear power dependence, so we attribute their origin to bound excitons. We note that other peaks such as biexcitons and dark excitons have been reported to appear within this lower energy range[5,6]. The sublinear power dependence is indicative of radiative combination of electrons and holes separately localized at different spatial sites[7]. L1 - L3 peak intensities rapidly quench above 100 K as thermal stimulation perturbs the weak interaction between the defect bounded excitons[8].

a

Mulliken Population Analysis

Structure	W	Se	$CHCl_3$
Pristine WSe_2	12.970	16.515	-
Cl-facing WSe_2	12.967	16.516	26.0125
H-facing WSe_2	12.953	16.523	26.03486

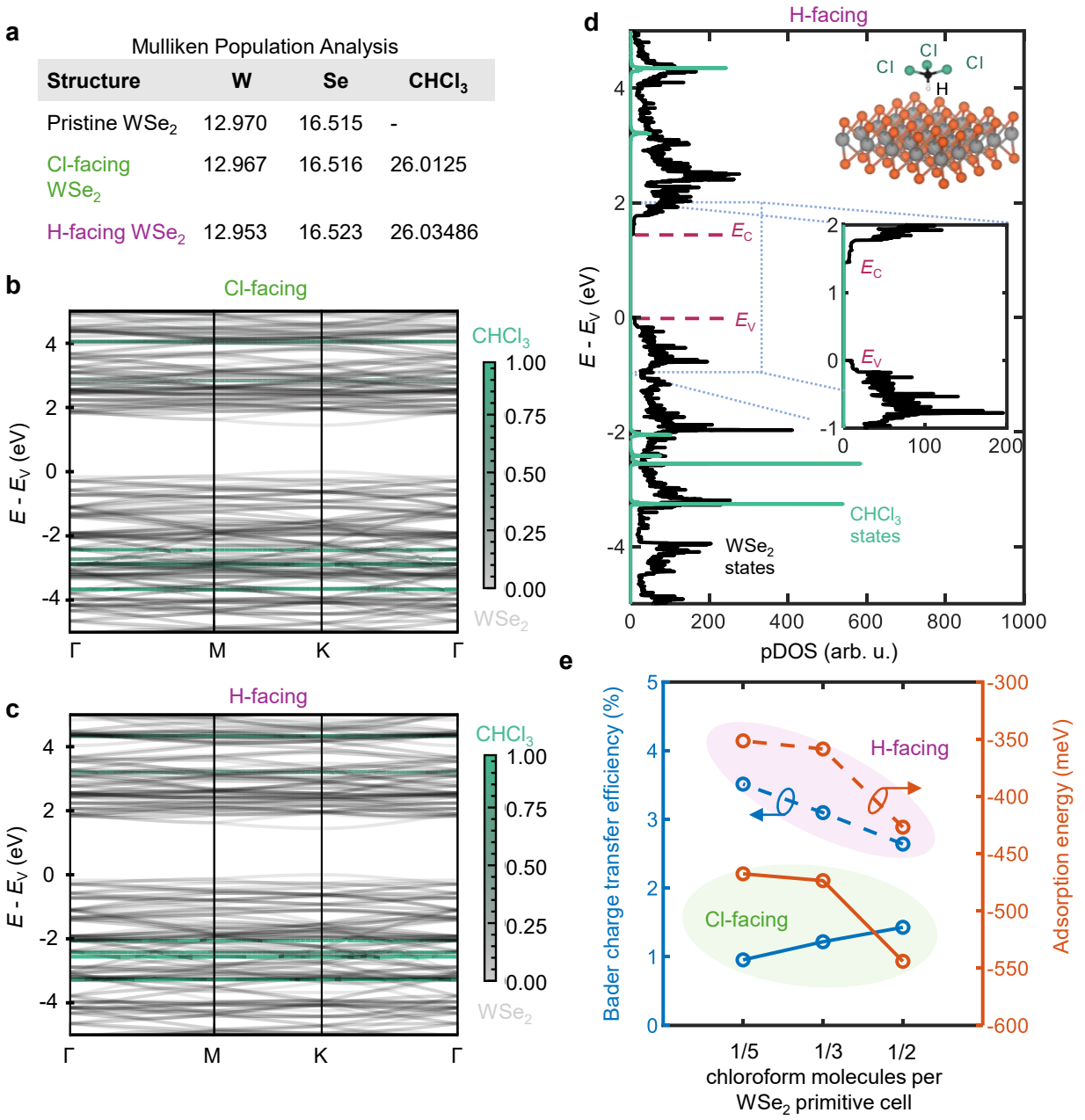

Supplementary Fig. 6 | Density Functional Theory Simulations. a, Mulliken population analysis of pristine and doped (Cl-facing and H-facing) monolayer WSe_2. The decrease in electron population of doped WSe_2 illustrates the *p*-doping of chloroform. Band structure of **b**, Cl-facing chloroform and **c**, H-facing chloroform interfaced with monolayer WSe_2. Transparent gray bands are contributions from monolayer WSe_2 and green bands are contributions from chloroform states. No chloroform states are formed in the WSe_2 band gap for both orientations. **d**, Projected density of states (pDOS) contributions from monolayer WSe_2 and chloroform to the overall DOS in the H-facing orientation. The valence band maximum E_V and conduction band minimum E_C are marked with dashed pink lines. The inset shows a zoomed-in view of the PDOS contributions around the WSe_2 bandgap. **e**, Charge transfer efficiency and adsorption energy with respect to chloroform coverage in both Cl-facing and H-facing orientations. A 2×2, 3×3, and 5×5 WSe_2 supercell were simulated with a chloroform molecule, corresponding to ½,⅓, and ⅕ chloroform molecules per WSe_2 primitive cell.

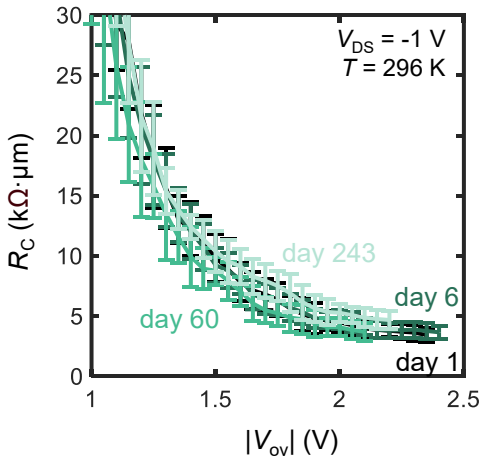

Supplementary Fig. 7 | Contact resistance (R_C) of chloroform-doped monolayer WSe_2 devices with Pd contacts 1 day, 6 days, 60 days, and 243 days (>8 months) after doping. Error bars indicate the standard error of the linear fit used for TLM extraction (fitting total resistance vs. L_{ch} at fixed V_{ov}), representing the uncertainty in the extracted R_C.

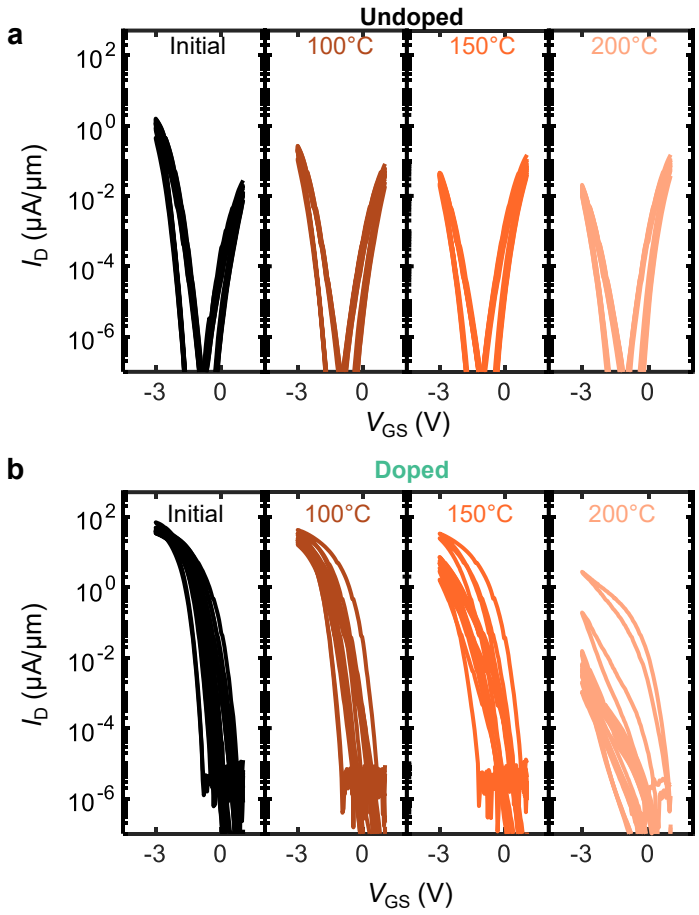

Supplementary Fig. 8 | Thermal Stability of L_{ch} = 1 μm Monolayer WSe_2 Devices. a, Measured I_D vs. V_{GS} initially and after annealing in vacuum at 100, 150, and 200°C. 9 devices were measured and plotted. **b,** Measured I_D vs. V_{GS} initially and after annealing in vacuum at 100, 150, and 200°C for chloroform-doped WSe_2. 14 devices were measured and plotted. For both plots, forward and backward sweeps are shown for all devices, and all devices demonstrate counterclockwise hysteresis.

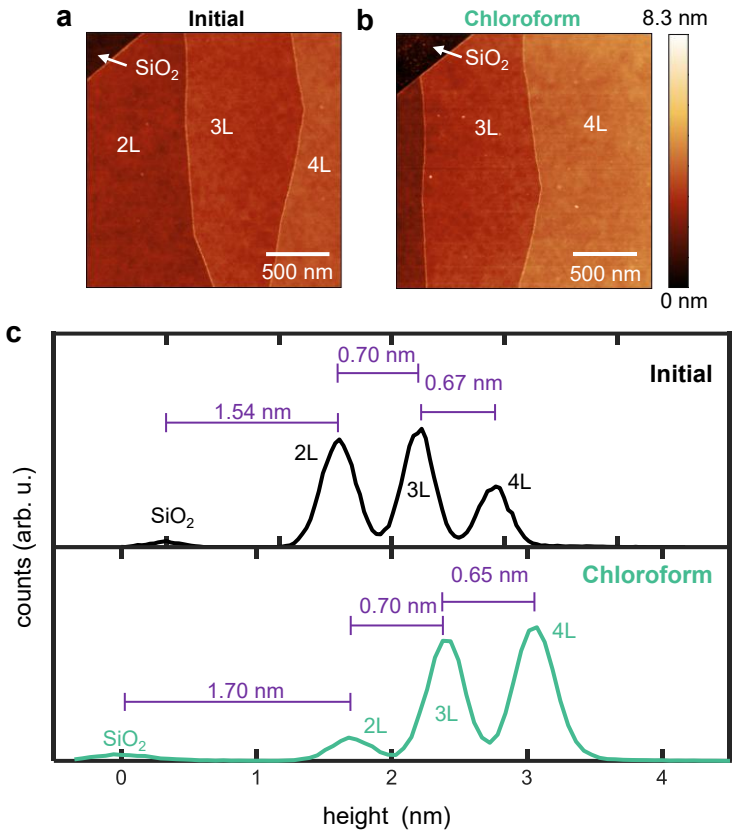

Supplementary Fig. 9 | Atomic Force Microscopy (AFM) of Exfoliated WSe_2. a, 2 × 2 μm^2 AFM scan of the 2-4L exfoliated WSe_2 flake in **Figure 5a** before doping. **b**, 2 × 2 μm^2 AFM scan of the 2-4L exfoliated WSe_2 flake in **Figure 5a** after chloroform doping. Some small particles can be identified on the flake after chloroform doping, similar to **Supplementary Fig. 2b**, but overall, there is minimal residue. **c**, Height distribution of the initial (top) and doped (bottom) AFM images in panel a and b, respectively. The peaks mark the height of the SiO_2, 2L, 3L, and 4L WSe_2 regions. There is no noticeable change in spacing between the WSe_2 layers, but the height difference between SiO_2 and 2L WSe_2 increases by > 0.15 nm. Gaussian curves were fit to the data to find the peak positions and peak separations.

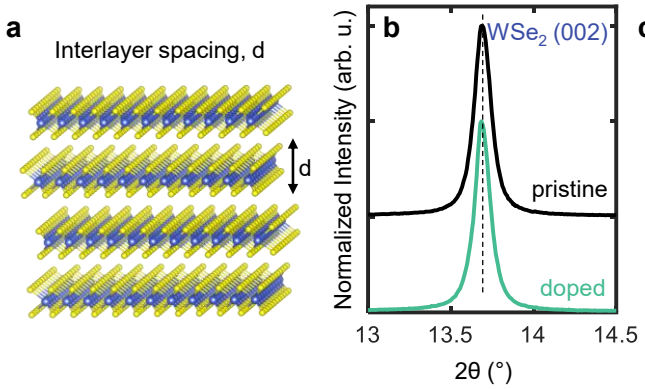

c

	2θ (°)	FWHM (°)	*d* (Å)
WSe_2 (pristine)	13.693	0.12	6.461
WSe_2 (doped)	13.689	0.11	6.463

Supplementary Fig. 10 | X-ray Diffraction (XRD) of Exfoliated Bulk WSe_2. **a**, Schematic of multilayer WSe_2 with interlayer spacing, *d*. **b**, X-ray diffraction spectra of multilayer WSe_2 (002) peak with and without chloroform doping. **c**, Calculated interlayer spacing and full-width half-maximum (FWHM) for the peaks in panel b.

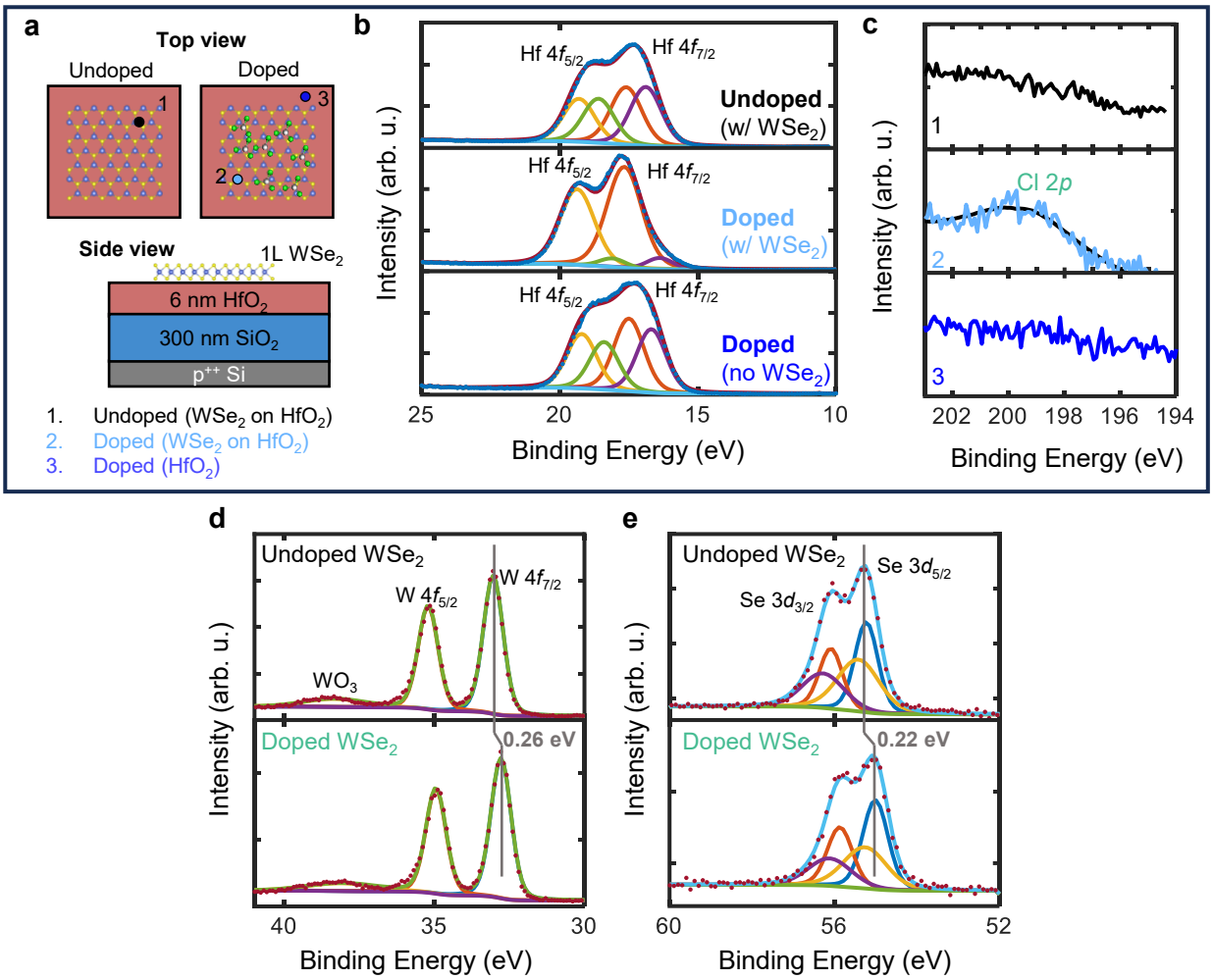

Supplementary Fig. 11 | X-ray Photoelectron Spectroscopy (XPS) of Monolayer WSe_2 on HfO_2. a, Representative schematic of 3 points probed by XPS: undoped WSe_2 on HfO_2, doped WSe_2 on HfO_2, doped HfO_2 sample with no WSe_2. HfO_2 was deposited by thermal atomic layer deposition, then underwent an O_2 plasma treatment prior to the WSe_2 transfer process (as described in Methods). **b**, XPS spectra of Hf 4*f* peaks at the 3 points located in panel a. The Hf 4*f* peaks shift to higher binding energy after exposure to chloroform. This could indicate the existence of chloroform near the HfO_2 surface, which then passivate interface traps and decrease the subthreshold swing. **c**, XPS spectra of the Cl 2*p* peak at the 3 points shown in panel a, indicating that the Cl peak exists only in the doped WSe_2 region. **d,** XPS spectra of W 4*f* peaks on undoped and doped WSe_2 on SiO_2. The W 4*f* peaks redshift by 0.26 eV, consistent with *p*-type doping. **e,** XPS spectra of Se 3*d* peaks on undoped and doped WSe_2 on SiO_2.The Se 3*d* peaks redshift by 0.22 eV. For the Se 3*d* peak fit, fitting the spectra with 2 instead of 4 peaks led to the same shift value. No new features or satellite features in the W 4*f* or Se 3*d* peaks were observed after doping. This suggests that the chloroform doping did not significantly change the chemical bonding environment for WSe_2, consistent with physisorption-dominated mechanism rather than covalent functionalization or substitution.

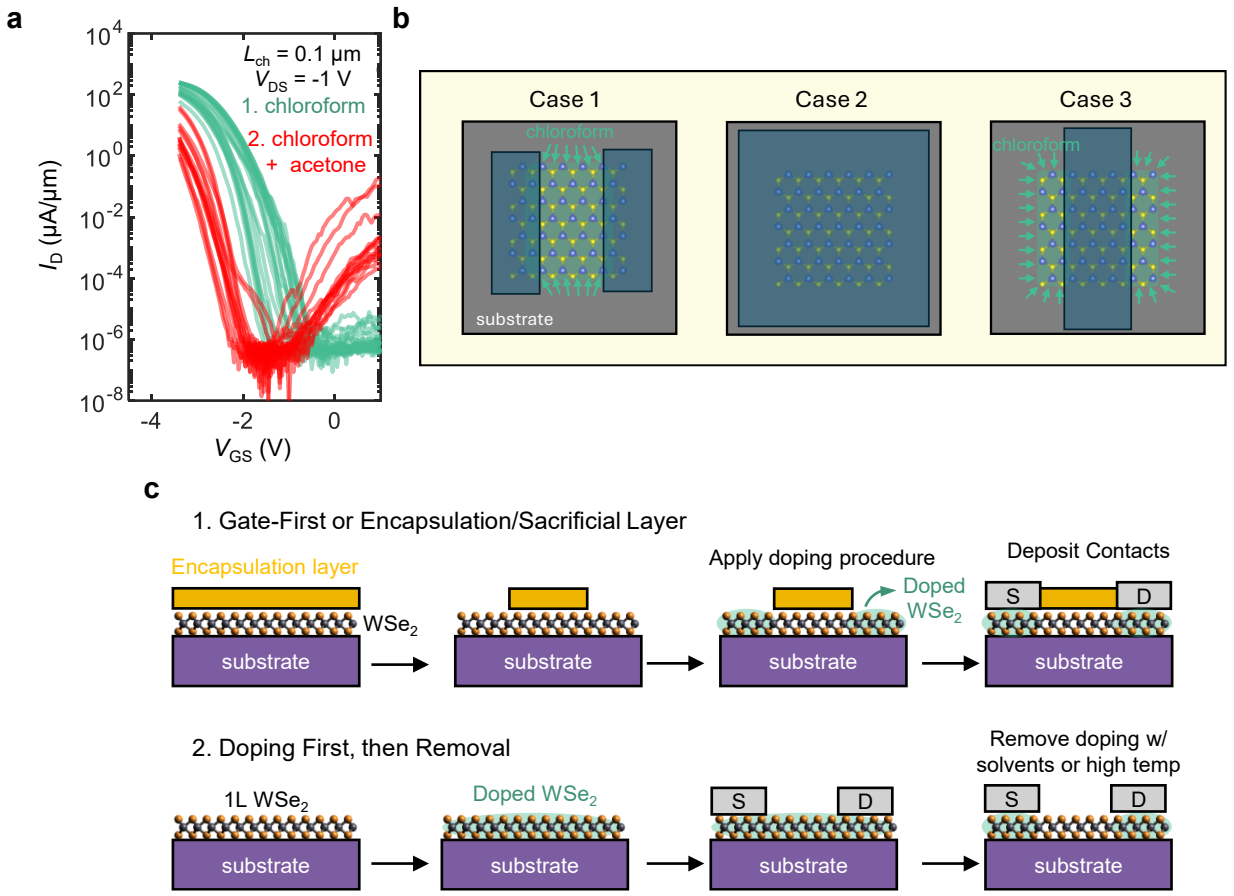

Supplementary Fig. 12 | Integration Challenges and Strategies. a, Measured I_D vs. V_{GS} curves of a monolayer WSe_2 device after doping with chloroform (green) and then after long (~8 hour) exposure to acetone (red). Devices revert back to similar currents as initial device performance (~1-10 μA/μm *p*-type drain current) and the *n*-branch re-emerges. **b,** Schematic illustrating possible chloroform intercalation pathways in WSe_2 devices with different geometries. The gray rectangle indicates the substrate, the atomic structure of a representative WSe_2 region is indicated, and blue regions indicate encapsulation by a metal or dielectric film covering the WSe_2. Chloroform intercalation pathways are indicated by green arrows. *Case 1* (left): chloroform could enter from the WSe_2 exposed edges and extend a finite distance beneath the encapsulated regions. *Case 2* (middle): In fully encapsulated geometries, no WSe_2 edges are exposed, and doping is expected to be blocked. *Case 3* (right): Partial encapsulation by oxide or metal may enable localized doping. **c**, Proposed process flows for selective-area doping with chloroform doping. Top: gate-first or encapsulation/sacrificial layer approach. Here, a sacrificial layer is first deposited, protecting the TMD from undesired doping. Doping is then selectively applied to un-protected regions. Bottom: doping then removal approach. Here, the dopant is first applied then selectively removed using high temperature processes or other solvents.

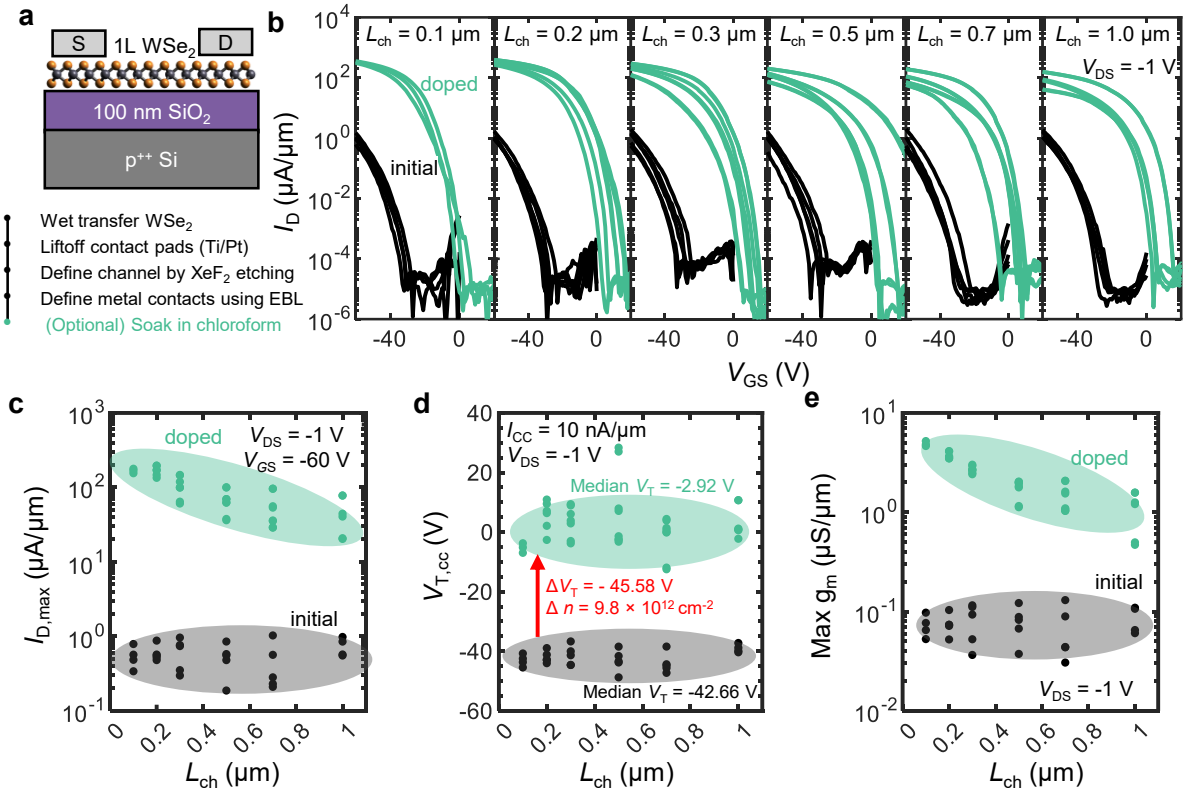

Supplementary Fig. 13 | Monolayer WSe_2 devices on 100 nm SiO_2 before and after chloroform doping. a, Cross-sectional schematic of WSe_2 transistor (top) and device fabrication procedure (bottom). Monolayer WSe_2 grown by chemical vapor deposition on sapphire was wet-transferred onto 100 nm SiO_2. Contact pads, channel regions, and fine contacts were defined using electron-beam lithography. Pd/Au contacts were used for fine contacts. **b**, Measured I_D vs. V_{GS} before and after doping at several channel lengths (L_{ch}) from 0.1 to 1 μm. **c**, L_{ch}-dependent statistical analysis before and after doping of maximum drain-current $I_{D,max}$ at V_{GS} = - 60 V. **d**, Threshold voltage ($V_{T,cc}$) at a constant current of 10 nA/μm before and after doping. The median V_T shift (ΔV_T) is - 45.6 V, corresponding to ~ 9.8 × 10^{12} cm^{-2} carriers induced (calculated from $\Delta n = C_{ox} \cdot \Delta V_T/q$. This closely matches the hole carriers induced on HfO_2 back-gates (**Supplementary Fig. 3b**). **e**, Maximum transconductance (g_m) vs. L_{ch} before and after doping.

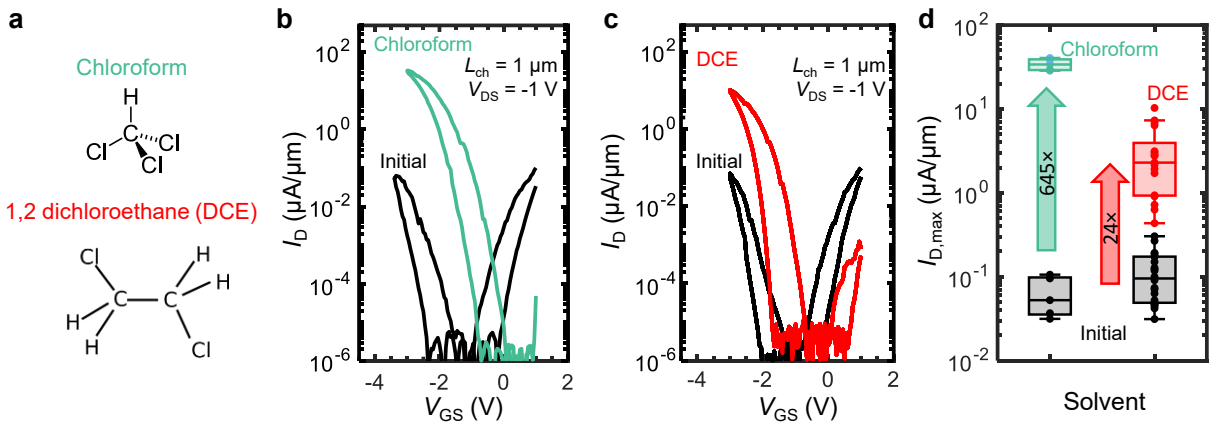

Supplementary Fig. 14 | Effect of Dichloroethane (DCE) as a *p*-type Dopant in Comparison to Chloroform. a, Diagram of a chloroform (top) and 1,2 dichloroethane (DCE) molecule (bottom). **b**, Measured I_D vs. V_{GS} curves of a monolayer WSe_2 device before and after doping with chloroform. Forward and backward sweeps are displayed with counter-clockwise hysteresis. **c** Measured I_D vs. V_{GS} curves of a monolayer WSe_2 device before and after doping with DCE. Forward and backward sweeps are displayed with counter-clockwise hysteresis. The devices were immersed overnight (> 8 hours) in dichloroethane (SIGMA-Aldrich, No. 34872) after device fabrication. **d**, Maximum drain-current ($I_{D,max}$) at V_{GS} = -3.0 V before and after doping with chloroform and DCE. Chloroform doped devices show >10× greater $I_{D,max}$ compared to DCE devices. All devices shown here are with L_{ch} = 1 µm. DCE increases the *hole* current of WSe_2 devices, with a median improvement in $I_{D,max}$ of ~24×, compared to the initial undoped WSe_2 devices. On the other hand, chloroform doping improves the hole current by ~ 645× on equivalent devices. The extra Cl atom in chloroform would increase the dipole moment of the dopant molecule, and thus could stabilize extra electrons, increasing the charge efficiency of chloroform. Additionally, the greater steric hinderance imposed by the larger DCE molecule suggests that it is much less likely to slip underneath the WSe_2. A box plot was created where the central mark of the box indicates the median, the bottom and the top edges of the box indicate the 25th and 75th percentiles, respectively.

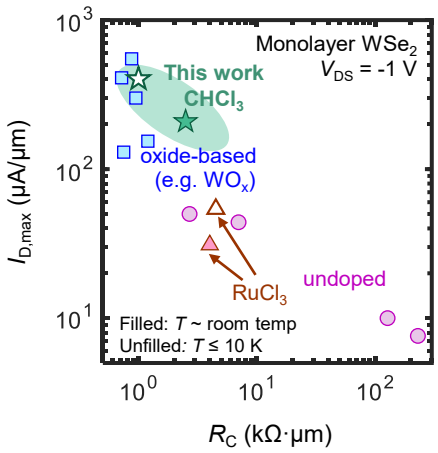

Supplementary Fig. 15 | Benchmarking maximum *p*-type current $I_{D,max}$ vs. contact resistance R_C for monolayer WSe_2 at V_{DS} = -1 V, using various contact metals and doping strategies. Circles mark results with no intentional doping[9–12], squares denote oxide-based doping (MoO_x, WO_x, NO_x)[3,13–17], and triangles label halide-based doping[18]. Filled markers indicate room temperature values and unfilled markers indicate low temperature < 10 K values. Our results with chloroform doping (stars) achieve among the highest hole currents and lowest contact resistance to date for monolayer WSe_2.

Supplementary Note 1: Estimating Initial Charge Before Chloroform Doping

To estimate the initial charge density in the WSe_2/HfO_2 stack, we use a simple analytical model[19], which derives a simple expression to estimate the threshold voltage V_T of an ultra-thin *n*-type transistor:

$$V_{\mathrm{T}} = \frac{\phi_{\mathrm{M}}}{q} - \frac{\chi_S}{q} - \frac{Q_{\mathrm{ss}}}{C_{\mathrm{ox}}} + \frac{Q_{\mathrm{sd}}}{C_{\mathrm{ox}}} \quad (1)$$

where ϕ_{M} is the metal work function, χ_{S} is the semiconductor electron affinity, q is the elementary charge, and Q_{ss} is the interfacial charge density. Q_{sd} is the depletion charge density, whose magnitude is proportional to the doping concentration (and is positive if the semiconductor is *p*-doped and negative if *n*-doped). We define the total initial (i.e., before doping with chloroform) charge density $Q_{\mathrm{total}} = Q_{\mathrm{sd}} - Q_{\mathrm{ss}}$, and rearrange the above equation to obtain:

$$Q_{\mathrm{total}} = Q_{\mathrm{sd}} - Q_{\mathrm{ss}} = \left(V_{\mathrm{T}} + \frac{\chi_{\mathrm{S}}}{q} - \frac{\phi_{\mathrm{M}}}{q}\right) C_{\mathrm{ox}} \quad (2)$$

To estimate Q_{total}, we use the measured transfer characteristics of the initial devices as seen in **Figure 2b.** The as-fabricated devices exhibit ambipolar *n*-type behavior, with the *n*-branch emerging near $V_{\mathrm{GS}} = 0$ V. We take an *n*-type $V_T \approx 1$ V at $L_{\mathrm{ch}} = 1$ μm from **Figure 2b** and $\chi_S = 3.9$ eV[20] for monolayer WSe_2. The work function of thin (8 nm) Pt films is $\phi_{\mathrm{M}} \approx 5.5$ eV[21], though 2 nm Ti in the gate stack could lower this; thus, we estimate that ϕ_{M} could be between 5.0 to 5.5 eV. With these values, and assuming an EOT of 2.4 nm (including the contribution from the van der Waals gap), we estimate $Q_{\mathrm{total}} \approx -1.4 \times 10^{-7}$ to -8.6×10^{-7} C·cm^{-2}, or approximately 9×10^{11} to 5×10^{12} charges per cm^2. Thus, upon chloroform doping, the induced hole density of ~10^{13} cm^{-2} (**Supplementary Fig. 3b**) compensates this initial electron density, dominating the final carrier concentration and shifting the device to *p*-type operation.

We stress that this is a very approximate range of Q_{total}, due to both approximations made when deriving equation (1) and uncertainties in the quantities used when calculating Q_{total} in equation (2). Further, we emphasize that the range calculated above is not merely the initial background doping concentration; rather, it is the difference between the charge density from doping and the immobile charge at or near the semiconductor/oxide interface. Although we are unable to separate these two terms, this range of Q_{total} still indicates an effective initial charge density that we anticipate will help others reproduce the results of this work.

While the precise initial carrier concentration may vary between WSe_2 sources, its influence on the final carrier density after doping is expected to be limited, as the doping process is primarily governed by adsorption and charge transfer rather than by the preexisting doping level. Consistent with this, the >100× increase in current after doping suggests that the induced carrier population substantially exceeds the initial carrier density.

Supplementary Table 1: Benchmarking the Electrical Performance of Monolayer WSe_2

Ref	Contact metal	Dopant	L_{ch} (nm)	I_{on} (μA/μm), $\lvert V_{DS}\rvert$ = 1 V	I_{on}/I_{off}	R_C (kΩ·μm)*	Stability (time, temperature)
9	Pd	-	600	10	10^8	127	-
10	Ru	-	200	50	2×10^7	2.7	-
22	Ru	-	100	100	10^8	-	-
11	Pt	-	1500	7.6	2×10^5	229	-
23	Pt/Au 10/80 nm	-	700	108.1	2×10^8	-	-
24	Ru/Au	-	70	247	10^8	-	-
25	Pt/Au 20/60 nm	-	200	15	10^7	-	-
26	TiO_2/Ru	-	140	100	10^8	-	-
27	Ru	-	50	92	10^8	-	-
13	Ti/Pd/Ni 1/30/30 nm	NO (175°C, 4 h)	65	300	2×10^6	0.95	16 days
			85	213			
			180	153			
			380	124			
14	Sb/Pt 10/12 nm	10 nm MoO_x	100	130	-	0.75	-
		-	100	30	10^6	-	-
28	Sb/Pt 10/12 nm	MoO_x	100	170	10^7	-	-
		-	100	66	10^7	-	-
29	Pd	WO_x	500	82	10^7	~1	-
		-	1000	27.6	10^7		-
15	Pd	5 nm MoO_x	50	410	~10^6	0.72	-
		-	200	170	~10^7		-
16	Ti/Pt/Au 0.5/30/30nm	2× WO_x, NO	55	550	~10^9	0.875	-
			180	188			-
			380	105			-
			780	82			-
		-	55	20	~10^8	-	-
17	Ti/Pt/Au 0.5/30/30nm	NO	55	300	10^9	0.875	24 days
30	Pd 25 nm	$HAuCl_4$ (50mM)	5500	100	10	-	-
		$HAuCl_4$ (5mM)	5500	8	10^7	-	-
3	Pd/Au 5/50 nm	WO_xSe_y	50	154	4×10^7	1.2	-
18	few layer graphene	α-$RuCl_3$	500	31	10^9	4.0 4.5 (at 10 K)	-
31	few layer graphene	α-$RuCl_3$	-	-	-	1.7 (at 300 mK, uniform doping), 20 (at 300 mK contact doping)	-
	Pt	α-$RuCl_3$	-	-	-	~ 36 (at 1.5 K)	-
This Work	Pd/Au 20/20 nm	$CHCl_3$	1000	119.2	10^{10}	2.5 1.0 (at 10 K)	243 days (8 months) 150 °C vacuum anneal
			700	153	10^{10}		
			500	163.2	10^{10}		
			300	184.9	10^{10}		
			200	201.5	10^{10}		
			100	208.7	10^{10}		

*R_C value given at room temperature if not otherwise stated

Blue text indicates *p*-type doping was implemented in the work

Supplementary References

1. Kang, D. H. *et al.* Controllable nondegenerate p-type doping of tungsten diselenide by octadecyltrichlorosilane. *ACS Nano* **9**, 1099–1107 (2015).
2. Borah, A., Nipane, A., Choi, M. S., Hone, J. & Teherani, J. T. Low-Resistance p-Type Ohmic Contacts to Ultrathin WSe_2 by Using a Monolayer Dopant. *ACS Appl. Electron. Mater.* **3**, 2941–2947 (2021).
3. Chen, S., Zhang, Y., King, W. P., Bashir, R. & van der Zande, A. M. Extension Doping with Low-Resistance Contacts for P-Type Monolayer WSe_2 Field-Effect Transistors. *Adv. Electron. Mater.* **11**, 2400843 (2025).
4. Varshni, Y. P. Temperature dependence of the energy gap in semiconductors. *Physica* **34**, 149–154 (1967).
5. Li, Z. *et al.* Revealing the biexciton and trion-exciton complexes in BN encapsulated WSe_2. *Nat. Commun.* **9**, 3719 (2018).
6. Tang, Y., Mak, K. F. & Shan, J. Long valley lifetime of dark excitons in single-layer WSe_2. *Nat. Commun.* **10**, 4047 (2019).
7. Huang, J., Hoang, T. B. & Mikkelsen, M. H. Probing the origin of excitonic states in monolayer WSe_2. *Sci. Rep.* **6**, 22414 (2016).
8. Wu, Z. *et al.* Defects as a factor limiting carrier mobility in WSe_2: A spectroscopic investigation. *Nano Res.* **9**, 3622–3631 (2016).
9. Dorow, C. *et al.* Advancing Monolayer 2-D nMOS and pMOS Transistor Integration from Growth to Van der Waals Interface Engineering for Ultimate CMOS Scaling. *IEEE Trans. Electron Devices* **68**, 6592–6598 (2021).
10. O'Brien, K. P. *et al.* Advancing 2D Monolayer CMOS Through Contact, Channel and Interface Engineering. in *2021 IEEE International Electron Devices Meeting (IEDM)* 7.1.1-7.1.4 (IEEE, 2021). doi:10.1109/IEDM19574.2021.9720651.
11. Wang, Y. *et al.* P-type electrical contacts for 2D transition-metal dichalcogenides. *Nature* **610**, 61–66 (2022).
12. Chou, S.-A. *et al.* Large-scale alkali-assisted growth of monolayer and bilayer WSe_2 with a low defect density. *Nat. Commun.* **16**, 2777 (2025).
13. Chiang, C.-C. *et al.* Air-Stable P-Doping in Record High-Performance Monolayer WSe_2 Devices. *IEEE Electron Device Lett.* **43**, 319 (2022).
14. Chou, A.-S. *et al.* High-Performance Monolayer WSe_2 p/n FETs via Antimony-Platinum Modulated Contact Technology towards 2D CMOS Electronics. in *2022 International Electron Devices Meeting (IEDM)* 7.2.1-7.2.4 (IEEE, 2022). doi:10.1109/IEDM45625.2022.10019491.
15. Chou, A.-S. *et al.* Status and Performance of Integration Modules Toward Scaled CMOS with Transition Metal Dichalcogenide Channel. in *2023 International Electron Devices Meeting (IEDM)* 1–4 (IEEE, 2023). doi:10.1109/IEDM45741.2023.10413779.
16. Lan, H.-Y., Tripathi, R., Liu, X., Appenzeller, J. & Chen, Z. Wafer-scale CVD Monolayer WSe_2 p-FETs with Record-high 727 μA/μm I_{on} and 490 μS/μm g_{max} via Hybrid Charge Transfer and Molecular Doping. in *2023 International Electron Devices Meeting (IEDM)* 1–4 (IEEE, 2023). doi:10.1109/IEDM45741.2023.10413736.
17. Lan, H.-Y. *et al.* Uncovering the doping mechanism of nitric oxide in high-performance P-type WSe_2 transistors. *Nat. Commun.* **16**, 4160 (2025).
18. Xie, J. *et al.* Low Resistance Contact to P-Type Monolayer WSe_2. *Nano Lett.* **24**, 5937–5943 (2024).

19. Jackson, T. Thinking MOSFETs. *IEEE Trans. Electron Devices* **72**, 1520–1522 (2025).
20. Liu, W., Cao, W., Kang, J. & Banerjee, K. (Invited) High-Performance Field-Effect-Transistors on Monolayer WSe_2. *ECS Trans.* **58**, 281–285 (2013).
21. Lee, W.-J. *et al.* Atomic Layer Deposition of Pt Thin Films Using Dimethyl (*N*, *N*-Dimethyl-3-Butene-1-Amine- *N*) Platinum and O_2 Reactant. *Chem. Mater.* **31**, 5056–5064 (2019).
22. Maxey, K. *et al.* 300 mm MOCVD 2D CMOS Materials for More (Than) Moore Scaling. in *2022 IEEE Symposium on VLSI Technology and Circuits (VLSI Technology and Circuits)* 419–420 (IEEE, 2022). doi:10.1109/VLSITechnologyandCir46769.2022.9830457.
23. Kim, K. S. *et al.* Non-epitaxial single-crystal 2D material growth by geometric confinement. *Nature* **614**, 88–94 (2023).
24. Penumatcha, A. *et al.* High Mobility TMD NMOS and PMOS Transistors and GAA Architecture for Ultimate CMOS Scaling. in *2023 International Electron Devices Meeting (IEDM)* 1–4 (IEEE, 2023). doi:10.1109/IEDM45741.2023.10413662.
25. Wang, X., Xiong, X., Shi, X., Gu, C. & Wu, Y. Optimized electrical properties of p-type field-effect transistors based on WSe_2 grown at moderate temperatures. *Appl. Phys. Lett.* **123**, (2023).
26. Dorow, C. J. *et al.* Exploring manufacturability of novel 2D channel materials: 300 mm wafer-scale 2D NMOS & PMOS using MoS_2, WS_2, & WSe_2. in *2023 International Electron Devices Meeting (IEDM)* 1–4 (IEEE, 2023). doi:10.1109/IEDM45741.2023.10413874.
27. Mortelmans, W. *et al.* Record Performance in GAA 2D NMOS and PMOS Using Monolayer MoS_2 and WSe_2 with Scaled Contact and Gate Length. in *2024 IEEE Symposium on VLSI Technology and Circuits (VLSI Technology and Circuits)* 1–2 (IEEE, 2024). doi:10.1109/VLSITechnologyandCir46783.2024.10631395.
28. Lin, Y.-T. *et al.* Antimony–Platinum Modulated Contact Enabling Majority Carrier Polarity Selection on a Monolayer Tungsten Diselenide Channel. *Nano Lett.* **24**, 8880–8886 (2024).
29. Hung, T. Y. T. *et al.* pMOSFET with CVD-grown 2D semiconductor channel enabled by ultra-thin and fab-compatible spacer doping. in *2022 International Electron Devices Meeting (IEDM)* vols 2022-December 7.3.1-7.3.4 (IEEE, 2022).
30. Ho, P. H. *et al.* High-Performance WSe_2 Top-Gate Devices with Strong Spacer Doping. *Nano Lett.* **23**, 10236–10242 (2023).
31. Pack, J. *et al.* Charge-transfer contacts for the measurement of correlated states in high-mobility WSe_2. *Nat. Nanotechnol.* **19**, 948–954 (2024).